

# Analysis of nonlocal neural fields for both general and gamma-distributed connectivities

Axel Hutt

Institute of Physics, Humboldt University of Berlin  
Newtonstr. 15, 12489 Berlin, Germany

Fatihcan M. Atay

Max Planck Institute for Mathematics in the Sciences  
Inselstr. 22, 04103 Leipzig, Germany  
[atay@member.ams.org](mailto:atay@member.ams.org)

Preprint. Final version in *Physica D* **203**, 30–54, 2005

## Abstract

This work studies the stability of equilibria in spatially extended neuronal ensembles. We first derive the model equation from statistical properties of the neuron population. The obtained integro-differential equation includes synaptic and space-dependent transmission delay for both general and gamma-distributed synaptic connectivities. The latter connectivity type reveals infinite, finite, and vanishing self-connectivities. The work derives conditions for stationary and nonstationary instabilities for both kernel types. In addition, a nonlinear analysis for general kernels yields the order parameter equation of the Turing instability. To compare the results to findings for partial differential equations (PDEs), two typical PDE-types are derived from the examined model equation, namely a general reaction-diffusion equation and the Swift-Hohenberg equation. Hence the discussed integro-differential equation generalizes these PDEs. In the case of the gamma-distributed kernels, the stability conditions are formulated in terms of the mean excitatory and inhibitory interaction ranges. As a novel finding, we obtain Turing instabilities in fields with local inhibition-lateral excitation, while wave instabilities occur in fields with local excitation and lateral inhibition. Numerical simulations support the analytical results.

**Keywords:** neuronal populations, synaptic connectivity, bifurcation analysis

**PACS:** 02.30.Rz, 87.18.Hf

## 1 Introduction

Understanding the basic mechanisms of neural activity is supposed to yield insights to major brain functions such as cognitive processes [1], motor coordination [2], or perception [3]. In addition, the understanding of pathological phenomena will support the clinical treatment of patients. Several studies in recent years indicate that some

of the known pathologies represent large-scale coherent phenomena originating from mutual activity of neural populations. We mention the hand tremor in Parkinson disease [4], epileptic seizures [5], or hallucinations. For instance, the latter frequently result from specific circumstances such as fatigue or sleep deprivation [6] and, in some cases, exhibit a shift of the neural state to an instability by increased neuronal excitation [7]. Ermentrout and Cowan [8] introduced a mesoscopic neuronal field theory and explained visual hallucination patterns by loss of stability at bifurcation points. Furthermore, external stimuli may also evoke coherent brain activity indicating synchronous neuronal activity on a mesoscopic spatial level [3, 9–12]. In this context, Freeman [13] has shown in an early work that encephalographic activity relates to mesoscopic dendritic currents. Dipole and current source density models support these findings [14]. These findings corroborate the study of mesoscopic models to gain further insights to brain activity.

Many authors studying mesoscopic neuronal activity treat synaptically coupled neuronal ensembles [15–25]. Our work follows the basic field approach of Jirsa and Haken [9], who combined the ensemble models of Wilson and Cowan [26] and Nunez [27]. This model considers a single type of neurons, which are interconnected by axons terminating at either excitatory or inhibitory synapses. Though the model accounts for the intrinsic delay due to axonal propagation, the delay does not affect temporal and spatial dynamics. An extended model introduces the synaptic response delay and thus adds a further time scale [28]. It turns out that the relation between synaptic and propagation delay affects the stability of the system. This model is equivalent to the model type studied extensively by several authors [8, 19, 29–32] neglecting axonal transmission delay. Further studies considering the transmission delay revealed novel criteria for the onset of wave instabilities [25, 28, 33–36] and confirmed its importance to traveling phenomena [37–39]. In addition to the temporal scales, the synaptic connectivity kernels define the spatial scales of the neuronal field. In most studies, these connectivity kernels exhibit their maximum at zero distances, i.e. strong self-connectivity.

The present work discusses the neural field dynamics by an analytical stability investigation for general connectivity kernels and taking into account the transmission delays. It extends a previous work [33] by several aspects. Firstly, more general stability conditions for non-oscillatory and oscillatory instabilities are derived and the derivation of the nonlinear order parameter equation for Turing instabilities is given in the case of general kernels. Furthermore, well-known partial differential equation (PDE) models are derived from the presented model. These derivations treat general connectivity kernels and thus extend previous studies assuming families of specific kernels [38, 40, 41]. Moreover, we point to experimental investigations on synaptic connections in mice, which reveal low probability of self-connections but an increased probability of connections at finite distance. Nunez described the corresponding histogram of connections mathematically by a gamma-function [27]. Further, he mapped this histogram to the connectivity histogram of human brains. These findings motivate us to focus on the family of gamma-distributed connectivity kernels, which exhibit divergent, finite, and negligible probability densities of self-connections for various parameters. We point out that in the latter cases the neural populations show a low probability of self-connections, while it is possible that few single cells exhibit self-connections. We examine how the different types of self-connections of populations affect the stability of neural activity. To our best knowledge, this treatment has not been done yet in a general way. The discussion

shows novel effects caused by divergent and vanishing population self-connections.

The paper is organized as follows. The subsequent section presents the derivation of the field equation. In section 3, conditions for both stationary and non-stationary instabilities are derived analytically for general kernels, followed by the derivation of the order parameter equation of the Turing instability. In addition, partial differential equations are derived from the model equation. Finally Section 4 applies the obtained results to the case of gamma-distributed kernels, followed by numerical simulations. Section 5 summarizes the results and closes the work.

## 2 The model

The present work follows a basic model approach treating the spatiotemporal dynamics of synaptically coupled neural populations. For decades, several authors have derived evolution equations of such neural ensembles (see e.g. [26, 42, 43] and [18, 44] for an overview). The present work applies the model of Amari [30] and Cowan [45], who discuss postsynaptic potentials in neural populations. In the following, this model is motivated and derived from the statistics of the neuron population in order to clarify its functional properties and its restrictions. The derivation follows some ideas of Amit [46].

### 2.1 Model derivation

Chemical synapses convert incoming action potentials to postsynaptic potentials (PSP) by emission of neurotransmitters [47]. Most excitatory synapses emit neurotransmitters called glutamate, which enhance the activity of the postsynaptic cells, while the neurotransmitter  $\gamma$ -aminobutyric (GABA) is emitted by inhibitory synapses and diminish the postsynaptic cell activity.

In a simplified model, synapses bind to dendrites which exhibit passive spread of current through its tissue. According to this approach, Freeman [48] was one of the first to show that the incoming action potentials mathematically convolute with an impulse response function  $h_e(t)$  and  $h_i(t)$  at excitatory and inhibitory synapses, respectively. This convolution reflects the linear response of synapses to pulse activity and involves a temporal delay. The present approach accounts for this finding and neglects both shunting effects and active dendritic processes.

In experimental practice single cell activation is measured frequently as the number of action potentials generated by membrane potentials exceeding a certain threshold potential during a fixed time interval. Hence it is reasonable to discuss the mean pulse rate at time  $t$  [26]. However, we remark that this replacement of sequences of actual spike trains is only justified if quantities relevant for the network dynamics are insensitive to trial-to-trial fluctuations, i.e. time coding of spikes is not relevant [17, 49]. This is given in case of uncorrelated single action potentials, which is assumed here.

In addition, the model introduces spatial patches or entities at the location  $x$ , which may be identified to neural macrocolumns [26, 27]. More specifically, such macrocolumns represent ensembles of interacting neurons, which evolve coherently. They are also called neuronal ensembles or neuronal pools [17, 50]. These pools have been found experimentally both in cortical [51, 52] and subcortical [53] areas. Subsequently, the

neural field discussed is built up by such spatial ensembles and thus are coarse-grained in space.

Consequently, excitatory and inhibitory PSPs  $\bar{V}^e$  and  $\bar{V}^i$ , respectively, averaged over a fixed time unit and the spatial area of a macrocolumn obey

$$\bar{V}^{e,i}(x, t) = \int_{-\infty}^t d\tau h_{e,i}(t - \tau) \bar{P}_{e,i}(x, \tau). \quad (1)$$

with  $h_{e,i}(t) = \bar{g}_{e,i}h(t)$ . Here,  $\bar{g}_e$  and  $\bar{g}_i$  represent the synaptic gain of excitatory and inhibitory synapses, respectively, averaged over a fixed time interval and averaged over a spatial patch (cf. [54,55]). In more detail,  $\bar{g}_e$  and  $\bar{g}_i$  are the synaptic coupling constants, which give the signal amplification of incoming pulse activity to excitatory and inhibitory postsynaptic potentials, respectively. Here the synaptic gains are homogeneous in space and time. Further,  $\bar{P}_e(x, t)$  and  $\bar{P}_i(x, t)$  represents the corresponding presynaptic pulse rate, which terminates at excitatory and inhibitory synapses, respectively.

The synaptic response behaviour is defined by the corresponding synaptic response functions  $h(t)$ . In the special case of  $h(t) \sim t \exp[-t]$ ,  $h(t)$  is the so-called alpha-function. However in more general mathematical terms,  $h(t)$  is the Green's function for the temporal operator  $\hat{L}$  with  $\hat{L}h(t) = \delta(t)$  and  $\delta(t)$  being the Dirac delta-function. Subsequently the integral equation (1) may be formulated as the ordinary differential equation

$$\hat{L}\bar{V}^{e,i}(x, t) = \bar{g}_{e,i}\bar{P}_{e,i}(x, t) \quad (2)$$

Further, Eq. (1) presumes that the synapses exhibit a larger time constant than the somatic membranes, which generate the received action potentials [18, 26, 56]. That is, the averaged PSPs  $\bar{V}^{e,i}$  evolve on a larger time scale than the pulse activity  $\bar{P}_{e,i}$ . Recalling the strong correlation of PSPs and encephalographic activity [57] the separation of membrane and synaptic time scales is reasonable as typical evoked encephalograms evolve at maximum frequencies of about 80Hz, i.e. minimum time scale  $\sim 12$ ms, while membrane time constants are in the range of 1 – 2ms. Further, this assumption is strongly related to the coarse-graining of temporal activity.

We point out that the assumptions made on the homogeneity of spatial patches and uncorrelated spike activity, i.e. slow population activity, are not valid in general. For instance some studies point to the importance of temporal correlations [36, 58], show fast population activity [59, 60] and reveal inhomogeneity in space, e.g. in prefrontal cortex of monkeys [61] or in the human visual cortex [62]. However, the assumptions made yield a simplified model that allows the study of principle mechanisms in neural tissue. For instance, recent work on the power spectrum of neural population activity [15, 16, 63, 64] explained successfully the power spectrum of experimental encephalographic data. Further, successful studies of spatial inhomogeneities are based on the proposed population model [61, 65].

Essentially, we assume variations of synaptic properties in the considered neuronal population [66]. Thus PSPs  $V^{e,i}(t)$  at single neurons become random variables with the corresponding probability distributions  $p_S^e(V^e - \bar{V}^e)$  and  $p_S^i(V^i - \bar{V}^i)$ . Since excitatory and inhibitory PSPs sum up at the trigger zone of each neuron [37], the probability

density function of the effective membrane potential  $V = V^e - V^i$  is

$$p_S(V - \bar{V}) = \frac{1}{2\pi} \int dz \phi_S^e(z) \phi_S^i(-z) e^{-izV}, \quad (3)$$

where  $\bar{V} = \bar{V}^e - \bar{V}^i$  and  $\phi_S^e, \phi_S^i$  are the characteristic functions of the corresponding probability density functions of  $p_S^e, p_S^i$ .

Now, we treat the conversion of membrane potentials to pulse activity. A single neuron generates an action potential, i.e. it fires, if the membrane potential  $V(t)$  at the trigger zone exceeds a certain threshold  $V_{th}$  at time  $t$ . Thus, the probability of a single neuron to fire is  $\Theta(V(t) - V_{th})$ , where  $\Theta$  denotes the Heaviside function. In addition, there are different types of neurons, e.g. short-range interneurons or pyramidal cells showing axonal connections on a longer range. In most cases, the former type inhibits synaptic activity, while the latter builds excitatory synaptic connections. For an ensemble of neurons at spatial location  $x$ , there is a distribution of firing thresholds  $D_k(V_{th} - \bar{V}_{th}, t)$  at time  $t$  subject to the neuron type  $k$ . Here  $D_k$  accounts for those neurons, who are not in a refractory period and thus can fire. Consequently  $D_k$  may change in time. Hence the expected number of firing neurons is

$$\begin{aligned} N_k(t) &= \int_{V_{min}}^{V_{max}} dV p_S(V - \bar{V}(t)) \int_{V_\ell}^{V_h} dV_{th} \Theta(V - V_{th}) D_k(V_{th} - \bar{V}_{th}, t) \\ &= \int_{V_{min} - \bar{V}}^{V_{max} - \bar{V}} dw \int_{V_\ell - \bar{V}_{th}}^{V_h - \bar{V}_{th}} du \Theta(w + \bar{V}(t) - \bar{V}_{th}) p_S(w) D_k(u, t). \end{aligned}$$

where  $\bar{V}_{th}$  denotes the mean firing threshold,  $V_{min}$  and  $V_{max}$  represent the minimum and maximum values of the membrane potentials, resp.,  $V_\ell$  and  $V_h$  denote the lowest and highest firing thresholds, resp., and  $p_S$  is taken from Eq. (3). Subsequently, the time-averaged pulse activity per unit time at time  $t$  at location  $x$  is given by

$$\begin{aligned} \bar{N}_k(t) &= \frac{1}{\Delta t} \int_t^{t+\Delta t} N_k(\tau) d\tau \\ &\approx \int_{V_{min} - \bar{V}}^{V_{max} - \bar{V}} dw p_S(w) \underbrace{\int_{V_\ell - \bar{V}_{th}}^{V_h - \bar{V}_{th}} du \Theta(w + \bar{V}(t) - \bar{V}_{th} - u) \bar{D}_k(u, t)}_{W(w, \bar{V}(t), t)} \quad (4) \end{aligned}$$

with the distribution of firing thresholds  $\bar{D}_k(u, t)$  per unit time  $\Delta t$  at time point  $t$ . Here, we assume slowly-varying PSPs on a time scale larger than  $\Delta t$ .  $\bar{N}_k(t)$  represents the average number of firing neurons of type  $k$  per unit time. In other words,  $\bar{N}_k(t)$  is the firing rate of the neural population at location  $x$  at time  $t$  and thus Eq. (4) is the general definition of the so-called transfer function. The case  $\bar{N}_k = 0$  represents the resting state of the neural field, i.e. the background activity. The definitions of the threshold distribution and firing rate are similar to the corresponding definitions of Wilson and Cowan [26].

Now, we examine the firing properties for different relations of the membrane potential and threshold borders. For simplicity, in the following we write  $\bar{V} = \bar{V}(t)$ ,

$\bar{D}_k(u) = \bar{D}_k(u, t)$  and assume implicitly the spatial location  $x$  and time  $t$ . From (4), we have  $W(w, \bar{V}) = 0$  for  $w + \bar{V} < V_\ell$ ,

$$W(w, \bar{V}) = \int_{V_\ell - \bar{V}_{th}}^{w + \bar{V} - \bar{V}_{th}} du \bar{D}_k(u) = F(w + \bar{V})$$

for  $V_\ell - \bar{V}_{th} \leq w + \bar{V} \leq V_h - \bar{V}_{th}$  and

$$W(w, \bar{V}) = \int_{V_\ell - \bar{V}_{th}}^{V_h - \bar{V}_{th}} du \bar{D}_k(u) = F_n$$

for  $w + \bar{V} > V_h$ . Here  $F(w + \bar{V})$  represents the number of non-refractory neurons with the thresholds  $w + \bar{V}$  per unit time at time  $t$ , and  $F_n$  denotes the total number of non-refractory neurons per unit time at time  $t$ . Our formulation generalizes a number of other models in the literature. This can be seen by examining several limiting cases. If  $V_{max} < V_\ell$  then  $\bar{N} = 0$ , i.e. the maximum membrane potential does not reach the lowest firing threshold, and thus there is no firing activity in addition to the background activity. In contrast, if  $V_{min} > V_h$  then  $\bar{N} = F_n$ . That is, all membrane potentials exceed the maximum firing threshold, each non-refractory neuron fires, and the number of firing neurons per unit time, i.e. the firing rate, is maximum. To further explain the distinction between the number of neurons per unit time with a fixed threshold and the firing rate, we interpret  $p_S$  as the probability that a threshold is actually reached. For instance, in the case of  $V_{min} > V_h$  the probability that the membrane potential exceeds the thresholds is equal to 1 and all participating neurons fire. A similar interpretation has been used in [26].

Another special situation occurs for  $V_{min} - \bar{V} \leq V_\ell - \bar{V}_{th} \leq V_h - \bar{V}_{th} \leq V_{max} - \bar{V}$ , leading to

$$\bar{N}(\bar{V}) = \int_{V_\ell - \bar{V}_{th}}^{V_h - \bar{V}_{th}} dw p_S(w) F(w + \bar{V}) + F_n \int_{V_h - \bar{V}_{th}}^{V_{max} - \bar{V}} dw p_S(w).$$

If  $p_S(w)$  is unimodal with maximum at  $w = 0$  and  $V_h \gg \bar{V}_{th}$ ,  $V_{max} \gg \bar{V}$ , then the last integral vanishes and the firing rate does not depend anymore on the borders of the membrane potentials. Furthermore, letting  $V_{max}, V_h \rightarrow \infty$  and  $V_\ell \rightarrow -\infty$  yields

$$\bar{N}_k(x, t) = \int_{-\infty}^{\infty} dw \int_{-\infty}^{w + \bar{V}(x, t) - \bar{V}_{th}} du p_S(w) D_k(u, t). \quad (5)$$

To be more specific, in the case of normally-distributed synaptic probability distributions  $p_S^{e,i}$ , the effective membrane potentials obey a normal distribution  $p_S \sim \mathcal{N}(0, \sigma_S^2)$ . Additionally, for Gaussian-distributed firing thresholds

$$\bar{D}_k(u, t) = \frac{P_{max}}{\sqrt{2\pi}\sigma_k} e^{-u^2/2\sigma_k^2},$$

the transfer function (5) and the nonlinear gain read

$$\bar{N}_k(x, t) = P_{max} \underbrace{\frac{1}{2} (1 + \operatorname{erf}(\frac{\bar{V}(x, t) - \bar{V}_{th}}{\sqrt{2}\eta_k}))}_{S_k(V(x, t))} \quad (6)$$

$$\frac{\partial \bar{N}_k(x, t)}{\partial \bar{V}} = \frac{P_{max}}{\sqrt{2\pi}\eta_k} e^{-(\bar{V}(x, t) - \bar{V}_{th})^2/2\eta_k^2},$$

respectively, where  $\eta_k^2 = \sigma_S^2 + \sigma_k^2$ ,  $\text{erf}(x)$  represents the Gaussian error function, and  $P_{max}$  denotes the maximum firing rate. By virtue of the probabilistic origin of  $\bar{N}_k(x, t)$ , it has a sigmoidal shape and the corresponding nonlinear gain reveals a maximum  $P_{max}/(\sqrt{2\pi}\eta_k)$ . We abbreviate the sigmoidal function by  $S_k(V)$  to indicate its shape. Equation (6) shows accordance to previous results [46] for a single neuron type.

Finally, the neural field contains axonal fibres, which link trigger zones to dendritic structures of distant terminal neurons. By virtue of these spatial connections, the corresponding nonlocal interactions yield temporal propagation delays in case of finite axonal propagation speeds  $v_e$  and  $v_i$ . Hence, the presynaptic pulse activities at excitatory and inhibitory synapses taken from Eq. (1) read

$$\begin{aligned} \bar{P}_e(x, t) &= \int_{\Omega} dy \left[ K_e^e(x, y) \bar{N}_e(y, t - \frac{|x-y|}{v_e}) + K_e^i(x, y) \bar{N}_i(y, t - \frac{|x-y|}{v_i}) \right] \\ &\quad + \mu_e I(x, t) \end{aligned} \quad (7)$$

$$\begin{aligned} \bar{P}_i(x, t) &= \int_{\Omega} dy \left[ K_i^e(x, y) \bar{N}_e(y, t - \frac{|x-y|}{v_e}) + K_i^i(x, y) \bar{N}_i(y, t - \frac{|x-y|}{v_i}) \right] \\ &\quad + \mu_i I(x, t), \end{aligned} \quad (8)$$

while  $\Omega$  denotes the spatial domain of the field. Here, the kernels  $K_b^a$  with  $a = e, i$ ,  $b = e, i$  denote the probability densities of synaptic connections from neurons of type  $a$  to synapses of type  $b$ . The additional pulse activity  $I(x, t)$  and the corresponding coupling factors  $\mu_{e,i}$  introduce an external input, e.g. from other cortical regions or from the midbrain [27].

## 2.2 The field equation

Now the derived model equations are combined to obtain the final evolution equation for excitatory and inhibitory neurons. Here, we presume excitatory (inhibitory) synaptic coupling of excitatory (inhibitory) neurons. After inserting Eqs. (7),(8) into Eq. (2), the membrane potential  $\bar{V} = \bar{V}^e - \bar{V}^i$  obeys

$$\begin{aligned} \hat{L}\bar{V}(x, t) &= \hat{L}\bar{V}^e(x, t) - \hat{L}\bar{V}^i(x, t) \\ &= \int_{\Omega} dy \bar{g}_e K_e(x, y) \bar{N}_e(y, t - \frac{|x-y|}{v_e}) + \bar{g}_e \mu_e I(x, t) \\ &\quad - \int_{\Omega} dy \bar{g}_i K_i(x, y) \bar{N}_i(y, t - \frac{|x-y|}{v_i}) - \bar{g}_i \mu_i I(x, t) \end{aligned}$$

with  $K_e = K_e^e$  and  $K_i = K_i^i$ . We take the spatial domain  $\Omega$  to be the real line. Additionally taking into account Eqs. (6) for both  $k = e$  and  $k = i$ , the final evolution equation becomes

$$\begin{aligned} \hat{L}V(x, t) &= \int_{-\infty}^{\infty} dy \left[ a_e K_e(x-y) S_e \left( V(y, t - \frac{|x-y|}{v_e}) \right) \right. \\ &\quad \left. - a_i K_i(x-y) S_i \left( V(y, t - \frac{|x-y|}{v_i}) \right) \right] + \mu I(x, t) \end{aligned} \quad (9)$$

with  $a_{e,i} = \bar{g}_{e,i} P_{max}$  and  $\mu = \bar{g}_e \mu_e - \bar{g}_i \mu_i$ . Moreover, the kernels are symmetric and homogeneous, i.e.  $K_{e,i}(x, y) = K_{e,i}(x-y) = K_{e,i}(|x-y|)$ .

### 3 Analysis for general kernels

This section aims to study the stability of a stationary state  $V_0$  which is constant in space and time. Here, we choose one type of neuron  $S_k = S_e = S_i = S$  and specify the impulse response function to  $h(t) = \alpha_1\alpha_2/(\alpha_2 - \alpha_1)(\exp(-\alpha_1 t) - \exp(-\alpha_2 t))\Theta(t)$ . After rescaling time to  $t \rightarrow t\sqrt{\alpha_1\alpha_2}$ , the temporal operator reads

$$\hat{L} = \left(\frac{\partial^2}{\partial t^2} + \gamma\frac{\partial}{\partial t} + 1\right) \quad (10)$$

with  $\gamma = \alpha_1/\alpha_2 + \alpha_2/\alpha_1 \geq 2$ . In the case of constant external input  $\mu I(x, t) = I_0$ , Eq. (9) gives the implicit equation for the stationary state  $V(x, t) = V_0$  as

$$V_0 = (a_e - a_i)S(V_0) + I_0. \quad (11)$$

Figure 1 illustrates its different solutions for  $a_e > a_i$  with respect to  $I_0$  as external control parameter. We mention the similarity to a cusp catastrophe [45].

For small deviations  $u(x, t) = V(x, t) - V_0 = u_0 e^{\lambda t + ikx}$ , the characteristic equation reads

$$L(\lambda) = s \int_{-\infty}^{\infty} dz \left( a_e K_e(z) e^{-\frac{\lambda}{v_e}|z|} - a_i K_i(z) e^{-\frac{\lambda}{v_i}|z|} \right) e^{-ikz} \quad (12)$$

with the nonlinear gain  $s = \delta S/\delta V$  at  $V = V_0$ . Here and in the following,  $\delta/\delta V$  denotes the functional derivative. Since  $I_0$  determines  $V_0$  and  $s$ , the nonlinear gain  $s$  represents the control parameter in the following.

When  $s = 0$ , one has  $L(\lambda) = \lambda^2 + \gamma\lambda + 1 = 0$ , so that  $\text{Re } \lambda < 0$  and the perturbations  $u$  are damped out. It follows that  $V_0$  is asymptotically stable for all small  $s$ , since the values  $(\lambda, k)$  satisfying the dispersion relation (12) depend continuously on  $s$ . However, increasing  $s$  further may result in a loss of stability; in this critical transition one has  $\text{Re } \lambda = 0$ . Thus setting  $\lambda = i\omega$  for some  $\omega \in \mathbf{R}$  in (12), we get

$$1 - \omega^2 + i\omega\gamma = s \int_{-\infty}^{\infty} dz \left( a_e K_e(z) e^{-i\omega|z|/v_e} - a_i K_i(z) e^{-i\omega|z|/v_i} \right) e^{ikz}. \quad (13)$$

Comparing the magnitudes of both sides,

$$\sqrt{(1 - \omega^2)^2 + \gamma^2\omega^2} \leq s \int_{-\infty}^{\infty} dz (a_e |K_e(z)| + a_i |K_i(z)|). \quad (14)$$

By simple calculus and the fact that  $\gamma \geq 2$ ,

$$(1 - \omega^2)^2 + \gamma^2\omega^2 \geq 1 \quad \text{for all } \omega \in \mathbf{R}. \quad (15)$$

Also by definition (cf. section 2)

$$\int_{-\infty}^{\infty} dz |K_{e,i}(z)| = 1. \quad (16)$$

Using (15) and (16) in (14), we obtain the necessary condition for loss of stability

$$1 \leq s(a_e + a_i). \quad (17)$$

Hence, the stationary state  $V_0$  is asymptotically stable for  $s < 1/(a_e + a_i)$ .

In order to investigate the dynamics of the nonlinear equation (9), it is useful to classify the different ways in which  $V_0$  may lose its stability as the parameter  $s$  is varied. In the following, we refer to stationary (Turing) and non-stationary instabilities in case the emerging spatio-temporal patterns are constant or changing in time, respectively. Stationary patterns are temporally constant, e.g. globally constant activation or periodic patterns in space. In contrast, non-stationary patterns are periodically oscillating in time, e.g. uniform global oscillations or traveling waves.

### 3.1 Stationary (Turing) instability

The stationary bifurcations are characterized by a solution pair  $(\lambda, k)$  of (12) with  $\lambda = 0$ , and the threshold for  $s$  becomes

$$s_c = \frac{1}{a_e \hat{K}_e(k_c) - a_i \hat{K}_i(k_c)} = \frac{1}{\hat{K}(k_c)} \quad , \quad k_c = \arg \min_k \hat{K}(k) \quad (18)$$

where  $\hat{K}_e$  and  $\hat{K}_i$  are the Fourier transforms, i.e. the characteristic functions, of the connectivity probability densities  $K_e$  and  $K_i$ , respectively.

In the case of a spatially constant bifurcation ( $k = 0$ ), the stationary state loses stability for

$$s > \frac{1}{\hat{K}(0)} = \frac{1}{a_e - a_i} \quad . \quad (19)$$

Figure 2 shows the corresponding bifurcation diagram for various parameters  $a_e, a_i$ . As mentioned in Section 2.1, the nonlinear gain  $s$  is constrained from above by  $s_m = 1/(\sqrt{2\pi}\eta)$ . It follows that if  $s_m < 1/(a_e - a_i)$ , then all stationary solutions are stable with respect to spatially constant bifurcations.

However, increasing  $s$  from zero, a non-constant bifurcation may emerge for  $\hat{K}(k) > \hat{K}(0)$  and  $(a_e + a_i) > \hat{K}(k_c) > (a_e - a_i)$  with  $k_c \neq 0$  and  $a_e > a_i$ . That is, Eq. (18) represents the condition for the instability onset with  $k \neq 0$ . The corresponding bifurcation has been found first by Turing in non-equilibrium activator-inhibitor systems [67, 68]. As mentioned in Section 2.1, the nonlinear gain  $s$  is constraint from above with maximum  $s_m = 1/(\sqrt{2\pi}\eta)$ . Subsequently, Turing bifurcations might occur only if  $\hat{K}(k_c) > 1/s_m \sim \eta$ , i.e. in case of small statistical variances of membrane potentials and firing thresholds. This additional condition relates the statistical field properties directly with the macroscopic behaviour.

### 3.2 Non-stationary instability

This type of bifurcation is characterized by a solution pair  $(\lambda, k)$  of (12) with  $\lambda = i\omega \neq 0$ . Hence these solutions describe oscillations at a nonzero temporal frequency  $\omega$ . We shall show that such bifurcations are possible only if the transmission speeds  $v_{e,i}$  are sufficiently small, and obtain an estimate to quantify this statement.

Considering the imaginary part of (13),

$$\begin{aligned} \omega\gamma &= -s \int_{-\infty}^{\infty} dz (a_e K_e(z) \sin(\omega|z|/v_e) - a_i K_i(z) \sin(\omega|z|/v_i)) \cos(kz) \\ &\quad + s \int_{-\infty}^{\infty} dz (a_e K_e(z) \cos(\omega|z|/v_e) - a_i K_i(z) \cos(\omega|z|/v_i)) \sin(kz). \end{aligned}$$

Note that the integrand in the first integral is an even function of  $z$  while that in the second integral is an odd function. Thus the second integral vanishes, and we have

$$\omega\gamma = -2s \int_0^\infty dz (a_e K_e(z) \sin(\omega z/v_e) - a_i K_i(z) \sin(\omega z/v_i)) \cos(kz)$$

which yields

$$|\omega|\gamma \leq 2s \int_0^\infty dz (a_e |K_e(z) \sin(\omega z/v_e)| + a_i |K_i(z) \sin(\omega z/v_i)|).$$

Using the fact that  $|\sin x| \leq |x|$  for all  $x$ , we obtain

$$|\omega|\gamma \leq 2s \int_0^\infty dz (a_e |K_e(z) \omega z/v_e| + a_i |K_i(z) \omega z/v_i|)$$

and since  $\omega \neq 0$  at a non-stationary bifurcation,

$$\gamma \leq s \left( \frac{a_e}{v_e} \int_0^\infty dz 2K_e(z)z + \frac{a_i}{v_i} \int_0^\infty dz 2K_i(z)z \right).$$

Note that the integrals are the definitions of the mean spatial interaction ranges

$$\xi_e = \int_{-\infty}^\infty dz |z| K_e(z) \quad , \quad \xi_i = \int_{-\infty}^\infty dz |z| K_i(z) \quad (20)$$

for excitatory and inhibitory connections. Hence we define  $\tau_e = \xi_e/v_e$  and  $\tau_i = \xi_i/v_i$  as the mean delay times respectively for the excitatory and inhibitory information transmission in the field. In this way, we can express a necessary condition for non-stationary bifurcations to occur, namely

$$s \geq s_c = \frac{\gamma}{a_e \tau_e + a_i \tau_i}. \quad (21)$$

Since all quantities are positive, it is clear that at least one of the velocities  $v_e$  or  $v_i$  must be finite for the occurrence of non-stationary bifurcations. These results generalize the findings in [33], which considers the case  $v_e = v_i$ . Furthermore, in some aspects it also generalizes previous results of Crook et al. [34] for networks of coupled oscillators. They revealed the importance of the ratio between spatial excitatory range and transmission speed for exponential kernels in the context of the oscillation stability. In contrast, the present findings generalize that ratio to general kernels for both excitation and inhibition.

With Eq. (21) and the previous condition  $1/(a_e + a_i) < s < 1/(a_e - a_i)$  for nonconstant bifurcations, the parameter regime for nonstationary bifurcation is given by

$$\frac{\gamma}{\tau_e \frac{a_e}{a_i} + \tau_i} < a_i s < \frac{1}{\frac{a_e}{a_i} - 1} \quad , \quad \frac{1}{\frac{a_e}{a_i} + 1} < a_i s$$

As can be shown by simple calculus, there is a threshold

$$a_e = \frac{\gamma + \tau_i}{\gamma - \tau_e} a_i \quad , \quad \tau_e < \gamma$$

beyond which no non-stationary bifurcations occur, while  $\tau_e > \gamma$  allows non-stationary bifurcations for all  $a_e \geq a_i$ . Figure 3 illustrates these findings, which extend previous results [33].

Finally, for large transmission speeds  $v_{e,i}$  one can carry out an asymptotic analysis following [33]. Let us consider the integral

$$\begin{aligned} \int_{-\infty}^{\infty} dz K(z) e^{-ikz} e^{-\lambda|z|/v} &= \int_{-\infty}^{\infty} dz K(z) e^{-ikz} \sum_{n=0}^{\infty} \frac{1}{n!} (-\lambda|z|/v)^n \\ &= \sum_{n=0}^{\infty} \frac{1}{n!} \int_{-\infty}^{\infty} dz K(z) |z|^n e^{-ikz} (-\lambda\epsilon)^n \\ &= \sum_{n=0}^{\infty} \frac{1}{n!} (-\lambda\epsilon)^n \hat{K}_n(k) \end{aligned}$$

with

$$\hat{K}_m(k) = \int_{-\infty}^{\infty} dz |z|^m K(z) e^{-ikz} = 2 \int_0^{\infty} dz z^m K(z) \cos(kz)$$

and  $\epsilon = 1/v$ . We use this series expansion in the characteristic equation (12), where, in case of local inhibitory and long-range excitatory connections, the delay due to inhibitory connections is neglected, i.e.  $1/v_i = 0$ . For excitatory and inhibitory kernels, large transmission speed  $v_e$  and  $\lambda = i\omega$ , we set  $1/v_e = \epsilon$ , and obtain by neglecting higher order terms  $\epsilon^n \forall n > 2$ ,

$$L(i\omega) \approx s\hat{K}(k) - i\omega a_e s \hat{K}_1^e(k)\epsilon - a_e \frac{\omega^2 s}{2} \hat{K}_2^e(k)\epsilon^2.$$

Finally the separation of real and imaginary part yields

$$s_{co} = -\frac{\gamma}{a_e \epsilon \hat{K}_1^e(k^*)} \quad , \quad \Omega^2 = 2 \frac{s_{co} \hat{K}(k^*) - 1}{a_e s_{co} \epsilon^2 \hat{K}_2^e(k^*) - 2} \quad (22)$$

That is, increasing  $s$  from zero the Hopf instability sets in at  $s_{co}$  with wave number  $k^*$ . In the case of  $k^* = 0$ , the emerging pattern exhibits global in-phase oscillations with oscillation frequency  $\Omega$ , while  $k^* \neq 0$  yields wave-like phenomena with phase speed  $v_{ph} = \Omega/k^*$ .

### 3.3 Nonlinear analysis of the Turing instability

In order to learn something about the nonlinear behaviour near the bifurcation point, this section aims at the nonlinear amplitude equation of the Turing instability. As shown in the previous examinations, the Turing bifurcation does not depend on the transmission speeds and thus we set  $v_e, v_i \rightarrow \infty$  in this section.

Expanding Eq. (9) to cubic nonlinear order about  $V_0$ , we obtain

$$\hat{L}u(x, t) \approx \int_{-\infty}^{\infty} dy K(x-y) [su(y, t) + \beta u^2(y, t) + \epsilon u^3(y, t)] \quad (23)$$

with  $u = V - V_0$ ,  $K = a_e K_e - a_i K_i$ ,  $\beta = (\delta^2/\delta V^2)/2$ , and  $\epsilon = (\delta^3/\delta V^3)/6$ , where the derivatives are computed at  $V = V_0$ .

Now we expand the field by the spatial eigenfunctions of the linear problem

$$u(x, t) = \int_{-\infty}^{\infty} dk \xi(k, t) e^{ikx} \quad (24)$$

with amplitudes  $\xi(k, t) = \xi^*(-k, t)$  and  $*$  denotes the complex conjugate. In the following,  $\xi(k, t)$  is abbreviated to  $\xi(k)$  for simplicity, while it remains time-dependent. Inserting (24) into (23) and integrating both sides over the space domain, we have

$$\begin{aligned} \hat{L}\xi(k) &= \frac{1}{2\pi} \int_{-\infty}^{\infty} dx e^{-ikx} [s \int_{-\infty}^{\infty} dk_1 \int_{-\infty}^{\infty} dy K(x-y) e^{ik_1 y} \xi(k_1) \\ &\quad + \beta \int_{-\infty}^{\infty} dk_1 \int_{-\infty}^{\infty} dk_2 \int_{-\infty}^{\infty} dy K(x-y) e^{iy(k_1+k_2)} \xi(k_1) \xi(k_2) \\ &\quad + \epsilon \int_{-\infty}^{\infty} dk_1 \int_{-\infty}^{\infty} dk_2 \int_{-\infty}^{\infty} dk_3 \int_{-\infty}^{\infty} dy K(x-y) e^{iy(k_1+k_2+k_3)} \xi(k_1) \xi(k_2) \xi(k_3)] \\ &= \frac{1}{2\pi} \int_{-\infty}^{\infty} dx e^{-ikx} [s \int_{-\infty}^{\infty} dk_1 \hat{K}(k_1) e^{ik_1 x} \xi(k_1) \\ &\quad + \beta \int_{-\infty}^{\infty} dk_1 \int_{-\infty}^{\infty} dk_2 \hat{K}(k_1+k_2) e^{ix(k_1+k_2)} \xi(k_1) \xi(k_2) \\ &\quad + \epsilon \int_{-\infty}^{\infty} dk_1 \int_{-\infty}^{\infty} dk_2 \int_{-\infty}^{\infty} dk_3 \hat{K}(k_1+k_2+k_3) e^{ix(k_1+k_2+k_3)} \xi(k_1) \xi(k_2) \xi(k_3)] \\ \hat{L}\xi(k) &= s\hat{K}\xi(k) + \beta\hat{K}(k) \int_{-\infty}^{\infty} dk_1 \xi(k_1) \xi(k-k_1) \\ &\quad + \epsilon\hat{K}(k) \int_{-\infty}^{\infty} dk_1 \int_{-\infty}^{\infty} dk_2 \xi(k_1) \xi(k_2) \xi(k-k_1-k_2)] \end{aligned} \quad (25)$$

Since  $\hat{L}$  is a temporal differential operator of second order, we write Eq. (25) as a system of two first-order differential equations

$$\dot{\xi}(k) = \eta(k) \quad (26)$$

$$\dot{\eta}(k) = (-1 + s\hat{K})\xi(k) - \gamma\eta(k) + N(\xi(k)), \quad (27)$$

where  $N(\cdot)$  represents the nonlinear terms in Eq. (25). Now we transform this equation system to a coordinate system with diagonal linear part by  $\mathbf{x}(k) = \mathbf{P}(k)\mathbf{y}(k)$ , where  $\mathbf{x}(k) = (\eta(k), \xi(k))^t$  and  $\mathbf{P}(k)$  is the  $2 \times 2$  transformation matrix. It follows that

$$\dot{\mathbf{y}}(k) = \mathbf{D}(k)\mathbf{y} + \mathbf{P}^{-1}(k)\mathbf{n}(\mathbf{y}(k)), \quad (28)$$

where  $\mathbf{n} = (0, N(\mathbf{y}))^t$ ,  $\mathbf{D}(k) = \mathbf{P}^{-1}(k)\mathbf{A}(k)\mathbf{P}(k)$  is a  $2 \times 2$  matrix and  $\mathbf{A}(k)$  represents the linear matrix in the system (26)-(27). The matrix  $\mathbf{D}$  is diagonal if the columns of  $\mathbf{P}$  contain the eigenvectors of matrix  $\mathbf{A}$ . The eigenvalues of  $\mathbf{A}$  are

$$\alpha(k) = \frac{1}{2}(-\gamma + \sqrt{\gamma^2 + 4(-1 + s\hat{K}(k))}), \quad (29)$$

$$\delta(k) = \frac{1}{2}(-\gamma - \sqrt{\gamma^2 + 4(-1 + s\hat{K}(k))}) < 0 \quad (30)$$

with corresponding eigenvectors  $\mathbf{v}(k) = (1, \alpha(k))^t$  and  $\mathbf{w}(k) = (1, \delta(k))^t$ . Since  $\alpha(k)$ ,  $\delta(k)$  are real and  $\det \mathbf{P}(k) \neq 0$  for all  $k$ , the coordinate transformation by  $\mathbf{P}(k)$  is valid. Thus the transformed differential equation system (26)-(27) reads

$$\dot{y}_1(k) = \alpha(k)y_1(k) - N(\mathbf{y}(k)) \quad (31)$$

$$\dot{y}_2(k) = \delta(k)y_2(k) + N(\mathbf{y}(k)) \quad (32)$$

with  $\mathbf{y} = (y_1, y_2)^t$ . By virtue of the properties of  $\alpha(k)$  and  $\delta(k)$ , the modes  $y_2(k)$  are stable for all  $k$ , while the  $y_1(k)$  are stable for  $(k - k_c)/k_c \gg 1$ . In contrast  $y_1(k)$  evolves on a much larger time scale near the Turing threshold  $s\hat{K}(k) = 1$ , i.e.  $k \approx k_c$  (cf. Eq.(18)). In the following, the latter modes are denoted  $z(k)$ , while the stable modes  $y_1(k)$  are renamed to  $s(k)$ . According the center manifold theorem [69],  $z(k)$  evolves on a center manifold, while the other modes obey  $y_2(k) = f_k(z(k))$  and  $s(k) = g_k(z(k))$  for some functions  $f_k, g_k$ . In more physical terms, the present separation of time scales near the bifurcation threshold yields a slaving mechanism and a circular causality [70]. That is, the modes  $z(k)$  slave  $y_2(k)$  and  $s(k)$ , while these slaved modes also determine the evolution of  $z(k)$ .

Now, we approximate  $f_k(z(k))$  and  $g_k(z(k))$  to lowest nonlinear orders and expand the nonlinear term in (31) to cubic polynomial order in  $z$ . Applying the introduced coordinate transformation  $\xi = y_1 + y_2$ ,

$$\dot{y}_2(k) = \delta(k)y_2(k) + \beta\hat{K}(k) \int_{-\infty}^{\infty} dk' z(k')z(k - k') \quad (33)$$

$$\dot{s}(k) = \alpha(k)s(k) - \beta\hat{K}(k) \int_{-\infty}^{\infty} dk' z(k')z(k - k') \quad (34)$$

$$\begin{aligned} \dot{z}(k) = & \alpha(k)z(k) - \beta\hat{K}(k) \int_{-\infty}^{\infty} dk' [z(k')z(k - k') + z(k')s(k - k')] \\ & + s(k')z(k - k') + z(k')y_2(k - k') + y_2(k')z(k - k') \\ & + \epsilon\hat{K}(k) \int_{-\infty}^{\infty} dk' \int_{-\infty}^{\infty} dk'' z(k'')z(k')z(k - k' - k'') \end{aligned} \quad (35)$$

Essentially after adiabatic elimination in Eq. (33) and (34) and inserting the results to Eq. (35), we find the order parameter equation

$$\dot{z}(k) = \alpha(k, s)z(k) + \Pi(k, s)z^3(k) \quad \forall k \approx k_c \quad (36)$$

by utilizing  $z(k) = z(-k)$ . In addition,

$$\Pi(k, s) = \hat{K}(k) [C\beta^2(s) + \epsilon(s)] \quad (37)$$

$$C = 2\hat{K}(0)\left(\frac{1}{\delta(0)} - \frac{1}{\alpha(0)}\right) + \hat{K}(2k_c)\left(\frac{1}{\delta(2k_c)} - \frac{1}{\alpha(2k_c)}\right) > 0. \quad (38)$$

In contrast to standard bifurcation theory, here both  $\alpha$  and  $\Pi$  depend on the control parameter  $s$ .

Recall that the general Turing instability exhibits stable stationary points  $z_{st} > 0$  for  $s > s_c$  due to nonlinear saturation, that is  $\Pi < 0$ . Figure 4 shows plots of  $\beta^2$  and  $\epsilon$  with respect to the control parameter  $s$ . It turns out that  $\Pi < 0$  and thus  $\epsilon < 0$

only if  $s$  exceeds a certain threshold. In this case, Eq. (36) describes the supercritical pitchfork bifurcation with the necessary nonlinear saturation. In contrast  $\Pi > 0$  yields no stable stationary solutions  $z_s > 0$  and both the applied quadratic approximations for the modes  $y_2(k)$  and  $s(k)$  and the adiabatic elimination procedure turn out being insufficient. That is, higher order polynomials need to be discussed.

We now focus on the case of  $\Pi < 0$ . Figure 5 presents plots of  $\Pi$  with respect to the bifurcation thresholds  $s_c$  for some  $\xi_e, \xi_i$ . For  $\Pi(s_c) < 0$ , pitchfork bifurcations occur at  $s \approx s_c$ . Figure 6 shows the bifurcation diagram of the stationary solution  $z_{st}$  with respect to  $\alpha$  (right panel) with  $z_{st} = \sqrt{\alpha(s)/[\hat{K}(k)(C\beta^2(s) + \epsilon(s))]}$ . The corresponding potential  $V_{pot}(z)$  with  $\dot{z} = -dV_{pot}/dz$  is plotted in Fig. 6 (left panel) for several values of the control parameter  $s$ .

### 3.4 Comparison to partial differential equations

To investigate the relation of the integro-differential equation (IDE) to partial differential equations (PDEs), we re-write the integral as

$$\begin{aligned} \int_{-\infty}^{\infty} dy K(x-y) S(V(y)) &= \int_{-\infty}^{\infty} d\eta K(\eta) S(V(x-\eta)) \\ &= \int_{-\infty}^{\infty} d\eta K(\eta) \sum_{n=0}^{\infty} (-1)^n \frac{1}{n!} \frac{\partial^n S(V(x-\eta))}{\partial(x-\eta)^n} \Big|_{x-\eta=x} \eta^n \\ &= \sum_{n=0}^{\infty} (-1)^n K_n \frac{\partial^n S(V(x))}{\partial x^n} \end{aligned} \quad (39)$$

with the kernel moments  $K_n = \int d\eta K(\eta) \eta^n \forall n \in \mathbf{N}$ . In the present work, the kernels are symmetric and thus  $K_n = 0$  for odd orders  $n$ .

It turns out that the expansion order  $n$  indicates the spatial interaction range. Typically, local or short-range PDE models involve spatial derivatives of up to second order, while PDE models with spatial derivatives of up to fourth order represent non-local or long-range models. The expansion (39) extends this classification to spatial derivatives of arbitrary order, while  $K_n$  gives the contribution of the nonlocal interactions of order  $n$ .

Now, we presume nonlocal interactions with  $K_n \rightarrow 0 \forall n > 4$ , and thus with spatial derivatives up to the fourth order. Then,

$$\begin{aligned} \int_{-\infty}^{\infty} dy K(x-y) S(V(y)) &\approx K_0 S(V(x)) + K_2 \frac{\delta^2 S}{\delta V^2} \left( \frac{\partial V}{\partial x} \right)^2 + K_4 \frac{\delta^4 S}{\delta V^4} \left( \frac{\partial V}{\partial x} \right)^4 \\ &\quad + K_2 \frac{\delta S}{\delta V} \frac{\partial^2 V}{\partial x^2} + 6K_4 \frac{\delta^3 S}{\delta V^3} \left( \frac{\partial V}{\partial x} \right)^2 \frac{\partial^2 V}{\partial x^2} \\ &\quad + 3K_4 \frac{\delta^2 S}{\delta V^2} \left( \frac{\partial^2 V}{\partial x^2} \right)^2 + 4K_4 \frac{\delta^2 S}{\delta V^2} \frac{\partial V}{\partial x} \frac{\partial^3 V}{\partial x^3} \\ &\quad + K_4 \frac{\delta S}{\delta V} \frac{\partial^4 V}{\partial x^4} \end{aligned} \quad (40)$$

In the following,  $K_n^e$  and  $K_n^i$  denote kernel moments for excitatory and inhibitory interactions, respectively. First, let us assume excitatory neurons which exhibit short but

non-vanishing interaction, while inhibitory connections are local only. In the case of  $S_i \gg S_e$ , the transfer function  $S_e$  for excitatory neurons expands to linear polynomial order about a fixed  $V_0$ . In the case of a temporal operator  $\hat{L}$  of first order and short range excitation  $K_{2n}^e \rightarrow 0 \forall n > 1$ , Eq. (9) becomes

$$\begin{aligned} \left(\frac{\partial u}{\partial t} + 1\right)u(x, t) &\approx K_0^e S_e(V_0) + sK_0^e u(x, t) + sK_2^e \frac{\partial^2 u}{\partial x^2} \\ &\quad - K_0^i S_i(u(x) + V_0) \\ \frac{\partial u}{\partial t} u(x, t) &= f(u) + D \frac{\partial^2 u}{\partial x^2} \end{aligned} \quad (41)$$

with  $s = \delta S_e / \delta V$  and the polynomial  $f(u) = K_0^e S_e(V_0) + sK_0^e u - K_0^i S_i(u + V_0)$ . Equation (41) is a reaction-diffusion equation with the diffusion coefficient  $D = sK_2^e$  and originates from the integro-differential equation (IDE) for short-range, linear excitatory interactions and nonlinear local inhibition.

In the case of longer excitatory interactions with  $K_{2n}^e \rightarrow 0 \forall n > 2$ , while expanding the transfer functions  $S_e$  and  $S_i$  to linear and third polynomial order about  $V_0$ , respectively, it is

$$\begin{aligned} \left(\frac{\partial}{\partial t} + 1\right)u(x, t) &\approx K_0^e S_e(V_0) + sK_0^e u(x, t) + sK_2^e \frac{\partial^2 u}{\partial x^2} + sK_4^e \frac{\partial^4 u}{\partial x^4} \\ &\quad - (K_0^i S_i(V_0) + sK_0^i u(x, t) + \beta K_0^i u^2(x, t) + \epsilon K_0^i u^3(x, t)) \end{aligned}$$

and finally after an affine transformation and scaling of time

$$\frac{\partial u(x, t)}{\partial t} = \bar{A}u(x, t) - \bar{B}u^2(x, t) - \bar{C}u^3(x, t) + \frac{\partial^2 u}{\partial x^2} + \frac{\partial^4 u}{\partial x^4}, \quad (42)$$

see Appendix A for more details. This PDE is a variant of the well-known Swift-Hohenberg equation [71–73]. Thus the modified Swift-Hohenberg equation represents a specific case of the IDE for long-range, linear excitatory interactions and cubic local inhibition.

## 4 Gamma-distributed kernels

In most previous works [8, 28, 43, 74, 75], neuronal fields exhibit axonal connections which are maximal at zero distance and monotonically decreasing for increasing distance. Then, the combination of excitatory and inhibitory axonal networks may yield four different spatial interactions, namely pure excitation, pure inhibition, local excitation-lateral inhibition, i.e. Mexican-hat, and local inhibition-lateral excitation, i.e. inverse Mexican-hat. In contrast, the current work picks up an interesting result of Nunez [27], who estimated the distribution of axonal cortico-cortical fiber lengths in humans based on distributions in mice. He found that cortico-cortical, i.e. excitatory, connections in humans may obey a gamma distribution with maximum at some centimeters. A similar problem has been addressed by Rinzel et al. [76], who found new propagation patterns in inhibitory networks with vanishing self-connections. Since there is also strong anatomical evidence for self-connections in inhibitory networks in cat visual cortex [77], we set the corresponding axonal distribution to a decreasing exponential.

## 4.1 Field properties

For gamma distributed connections, the connection probability densities read

$$K_e(x, y) = \frac{1}{2r_e^p \Gamma(p)} |x - y|^{p-1} e^{-|x-y|/r_e}, \quad K_i(x, y) = \frac{1}{2r_i} e^{-|x-y|/r_i} \quad (43)$$

where  $p > 0$  is a parameter of the gamma distribution,  $\Gamma(p)$  denotes the gamma function and  $r_e, r_i$  are the spatial ranges of excitatory and inhibitory connectivity kernels, respectively. After scaling  $t \rightarrow t\sqrt{\alpha_1\alpha_2}$ ,  $x \rightarrow x/r_e$ ,  $v_{e,i} \rightarrow v_{e,i}/(r_e\sqrt{\alpha_1\alpha_2})$ , we get

$$K_e(x) = \frac{1}{2\Gamma(\xi_e)} |x|^{\xi_e-1} e^{-|x|}, \quad K_i(x) = \frac{1}{2\xi_i} e^{|x|/\xi_i}, \quad (44)$$

with  $\xi_e = p$ ,  $\xi_i = r_i/r_e$  taken from (20). The temporal operator  $\hat{L}$  is taken from section 3, and furthermore  $S_e = S_i = S$ .

In most studies treating spatial structures in neuronal fields, excitatory and inhibitory connectivity kernels are of the same functional type such as exponentials or Gaussians. In these models, the excitation and inhibition comes in by different spatial scales, say  $r_e, r_i$ . In consequence, the spatial interaction ranges can be scaled to  $\xi_e = 1$  and  $\xi_i \neq 1$ . That is, the single parameter  $\xi_i$  reflects the relation of the excitatory and the inhibitory spatial scale and thus defines the spatial interaction. In contrast, Eq. (43) introduces the additional parameter  $p$  yielding two variables. Now  $\xi_i \neq 1$  still gives the relation of excitation and inhibition, while  $\xi_e$  is related to the excitatory self-interaction.

To be more precise, Figure 7 shows both kernels for various parameters  $\xi_e$ ,  $\xi_i$  and we observe singular self-excitations for  $\xi_e < 1$  (Fig. 7, left panel). At a first glance, this singularity of the probability density  $K_e$  may appear unphysical. However, this effect occurs even in much more simple processes and we mention the standard Brownian motion exhibiting a singular probability density of sojourn times [78, 79]. In addition,  $\xi_e > 1$  leads to  $K_e(0) = 0$ , while the maximum of  $K_e(x)$  is located at  $x_0 = \xi_e - 1$ . In other words, the self-excitation vanishes and the maximum connectivity is reached at the distance  $x_0$  from the origin. Subsequently by considering the inhibitory kernel,  $\xi_e < 1$  yields local inhibition with the self-interaction  $a_e K_e(0) - a_i K_i(0) = -a_i/\xi_i^2$  for all  $\xi_i$  and  $a_e, a_i > 0$ , while  $\xi_e > 1$  reflects local excitations for all  $\xi_i$  and  $a_e, a_i > 0$ . These cases contrast to the well-known case  $\xi_e = 1$ , which facilitates both local excitation and inhibition subject to  $a_e/a_i$  and  $\xi_i$ .

## 4.2 Stationary (Turing) instability

For the special choice of kernels (44), the condition for the Turing instability (18) is  $s_c = 1/\hat{K}(k_c)$ , with

$$\hat{K}(k) = \frac{a_e}{\sqrt{1+k^2}^{\xi_e}} \cos(\xi_e \arctan(k)) - \frac{a_i}{1+\xi_i^2 k^2}.$$

Since  $s_c > 0$  and  $\hat{K}(k) \rightarrow 0$  as  $k \rightarrow \infty$ ,  $\hat{K}(k_c)$  represents a positive local maximum for finite  $k_c$ . The corresponding sufficient condition reads

$$\frac{\partial^2 \hat{K}(k)}{\partial k^2} \Big|_{k=0} > 0 \Rightarrow \xi_i^2 > \frac{a_e}{2a_i} \xi_e (\xi_e + 1) \quad (45)$$

with

$$\frac{\partial^2 \hat{K}(k)}{\partial k^2} = -\frac{a_e \xi_e (\xi_e + 1)}{\sqrt{1 + k^2}^{\xi_e + 2}} \cos((\xi_e + 2) \arctan(k)) + 2a_i \xi_i^2 \frac{1 - 3\xi_i^2 k^2}{(1 + \xi_i^2 k^2)^3}.$$

Figure 8 shows the corresponding parameter space.

In the case of  $a_e > a_i$  and  $\xi_e < 1$ , Turing patterns occur only for  $\xi_i > \xi_e$  (Fig. 9), i.e. for larger mean inhibitory interaction than mean excitatory interaction. This behaviour shows accordance to previous findings. However, for  $\xi_i < \xi_e$  we find also Turing instabilities with the additional condition  $\xi_e \geq (a_e/a_i)/(2 - a_e/a_i)$ . That is, Turing patterns occur even for local inhibitory interactions, which has not been found in previous works. In the case of  $a_e < a_i$ , Turing patterns might also occur for  $\xi_i < \xi_e$  and  $\xi_e \geq (a_e/a_i)/(2 - a_e/a_i)$ .

Figure 10 shows the effective kernel  $a_e K_e(x) - a_i K_i(x)$  and corresponding Fourier transform  $\hat{K}(k)$  for both  $\xi_e = 1$  and  $\xi_e = 2.0$ . We observe that the kernels exhibit local excitation-lateral inhibition interaction with  $\xi_e = 1$ , while for  $\xi_i > 1$  Turing instabilities may also occur for  $\xi_e = 2$  although the kernel elicits local inhibition-lateral excitation interaction. Eventually recalling the findings of Nunez [27], experiments indicate intracortical inhibitory connections with  $r_i \approx 1\text{mm}$  and cortico-cortical connections with  $r_e = 20\text{mm}$ , i.e.  $\xi_i = 0.05$ . In addition,  $a_e > a_i$  and  $\xi_e = 3$ . Subsequently, according to Eq. (45) and Fig. 8, Turing patterns do not occur for these parameters and have not been found in experiments yet.

### 4.3 Non-stationary instability

According to section 3.2, the bifurcation threshold  $s_{co}$  for oscillatory instabilities depends strongly on the kernel Fourier moments  $\hat{K}_m$ . For the kernels (44), these moments are

$$\begin{aligned} \hat{K}_m^e(k) &= \frac{\Gamma(\xi_e + m)}{\Gamma(\xi_e) \sqrt{1 + k^2}^{(\xi_e + m)}} \cos((\xi_e + m) \arctan(k)) \\ \hat{K}_m^i(k) &= \frac{\Gamma(m + 1) \xi_i^m}{\sqrt{1 + k^2}^{(m + 1)}} \cos((m + 1) \arctan(\xi_i k)). \end{aligned}$$

Figure 11 shows plots of  $v_{ph}$  with respect to  $v_e$  for various  $\xi_e, \xi_i$ . We point out that the phase speed is smaller than the transmission speed in accordance to previous experimental [80] and theoretical results [28, 33]. In contrast to previous findings, there are also oscillatory instabilities for  $\xi_e < 1$ , i.e. in local excitation-lateral inhibition fields.

### 4.4 Numerical simulation

For the numerical investigations, Eq. (6) is approximated by the logistic function  $\bar{N} = P_{\max}/(1 + \exp(-1.8(V - 3.0)))$  [81]. The synaptic parameters are set to  $\alpha_1/\alpha_2 = 1.46$  i.e.  $\gamma = 2.1$ , while the propagation speed along excitatory axonal connections is set to  $v_e = 10$ , and the delay corresponding to short-range inhibitory connections is neglected. The subsequent temporal integration procedure applies an explicit Euler algorithm with time increment  $dt$  while the spatial integration algorithm represents an adaptive integration procedure. This algorithm divides the integration region into subintervals, and on each

iteration the subinterval with the largest estimated error is bisected. Each interval is integrated according to the 61 point Gauss-Kronrod rules [82]. Further, periodic boundary conditions are set yielding the integration rule

$$\int_{-\infty}^{\infty} K(|x-y|)f(y)dy \approx \int_0^L K(L/2 - |L/2 - |x-y||)f(y)dy.$$

with  $L = Ndx$ .

The first simulation aims to verify the Turing instability found analytically in section 3.3. Figure 12 presents the Turing instability by a space-time plot for initial values  $V^0(x, t) = V_0 + 0.5(\cos(0.5k_c x) + \cos(k_c x) + \cos(2.0k_c x))$  for  $L/v_e \leq t \leq 0$  with the critical wave number  $k_c = 0.589$ .

Finally to verify the novel findings of the section 4.2, we simulate the field activity for  $\xi_e = 2.0$  and  $\xi_i = 1.92$  with the same initial conditions. Figure 13 presents the corresponding space-time plot, which confirms the Turing instability for local inhibition-lateral excitation fields.

Since too large time increments used in the Euler algorithm may destabilize the numerical solutions, we check on various time increments  $0.005 \leq dt \leq 0.1$ . For  $dt \leq 0.05$ , the corresponding results verify the plots in Figs. 12 and 13.

## 5 Conclusion

This study derives the neural population model from statistical neural properties and analyses the resulting integro-differential equation (IDE) with respect to the stability of its equilibrium solutions. The first part of the analysis gives conditions for stationary and non-stationary instabilities. It is shown that the stationary bifurcation threshold is independent of the transmission speed and is mainly defined by the Fourier transforms of the excitatory and inhibitory connectivity kernels. This result yields the condition for the onset of Turing instabilities. In turn, the non-stationary bifurcations strongly depend on the mean interaction time of excitatory and inhibitory connections, where the interaction time represents the ratio of the mean interaction range to the transmission speed. Furthermore, a perturbation analysis for large transmission speeds yields the bifurcation threshold for Hopf-instabilities, the corresponding wave number, and the phase velocity of the emerging wave instabilities. Here, the bifurcation threshold depends mainly on the introduced excitatory and inhibitory kernel Fourier moments.

To gain further information on the existence of instabilities, the nonlinear order parameter equation for Turing patterns is derived and discussed in some detail. It turns out that the order parameter obeys a pitchfork bifurcation. A subsequent comparison of the model to partial differential equations reveal the relation to reaction-diffusion models and a variant of the Swift-Hohenberg equation. Hence, these PDEs can be considered as special cases of the single IDE.

Finally, the analysis of gamma-distributed excitatory kernels reveals Turing instabilities for local inhibition-lateral excitation fields and wave instabilities for local excitation-lateral inhibition fields. These novel findings contrast to previous results and originate from the vanishing and divergent self-excitation. Since the examined gamma-distributions are based on experimental findings, our results reveal a new mechanism for global traveling brain waves.

The presented study is a step in generalizing the analysis of non-locally interacting neural fields towards obtaining a classification scheme for observed spatio-temporal patterns. We mention the important generalization of Kishimoto and Amari [31] in lateral-inhibition type fields in the absence of transmission delay. Since neurophysiological properties of observed neural tissue are not accessible precisely, a classification scheme should be useful in connecting model functionals to observed phenomena. For example, observed traveling waves necessitate a mean interaction time beyond a certain threshold defined by synaptic kernel properties. In addition, this classification might be important for estimating interaction parameters from multi-site neuronal data [83]. Future studies in this area could incorporate additional mechanisms like standing and traveling pulse fronts [25, 84] or the consideration of feedback delay [85–87].

## Appendix

### A Transformation to modified Swift-Hohenberg equation

In section 3.4, the PDE (42) may be written as

$$\begin{aligned}\frac{\partial u(x,t)}{\partial t} &= A + Bu(x,t) - Cu^2(x,t) - Du^3(x,t) + E\frac{\partial^2 u(x,t)}{\partial x^2} + F\frac{\partial^4 u(x,t)}{\partial x^4}. \\ A &= K_0^e S_e(V_0) - K_0^i S_i(V_0) \quad , \quad B = sK_0^e - sK_0^i - 1 \\ C &= \beta K_0^i \quad , \quad D = \epsilon K_0^i \quad , \quad E = sK_2^e \quad , \quad F = sK_4^e.\end{aligned}$$

Introducing the new variable  $z(x,t) = u(x,t) + k$  with an arbitrary constant  $k$  in space and time, the PDE can be transformed to

$$\begin{aligned}\frac{\partial z(x,t)}{\partial t} &= az(x,t) - bz^2(x,t) - Dz^3(x,t) + E\frac{\partial^2 z(x,t)}{\partial x^2} + F\frac{\partial^4 z(x,t)}{\partial x^4}. \\ a &= B + 2Ck - 3Dk^2 \quad , \quad b = 3Dk - C\end{aligned}$$

if  $k$  is a root of  $A - Bk - Ck^2 + Dk^3 = 0$ . Finally we re-scale space by  $x \rightarrow x/r$  and subsequently time by  $t \rightarrow tF/r^2$ , while  $r$  is an arbitrary spatial scale. Then the modified Swift-Hohenberg equation (42) is obtained with the choice  $r = \sqrt{F/E}$  and the abbreviations  $\bar{A} = aF/E^2$ ,  $\bar{B} = bF/E^2$  and  $\bar{C} = DF/E^2$ .

## Acknowledgements

A. Hutt has been supported by the DFG Research Center "Mathematics for key technologies" (Matheon) in Berlin, Germany. Further the authors would like to thank the anonymous reviewers for valuable comments.

## References

- [1] M. S. Gazzaniga, editor. *The new cognitive neurosciences*. MIT Press, Cambridge, 2000.
- [2] J. A. S. Kelso. *Dynamic Patterns: The Self-Organization of Brain and Behavior*. MIT Press, Cambridge, 1995.
- [3] W. J. Freeman. *Neurodynamics: An Exploration in Mesoscopic Brain Dynamics (Perspectives in Neural Computing)*. Springer-Verlag, Berlin, 2000.
- [4] P. Tass. *Phase resetting in medicine and biology : stochastic modelling and data analysis*. Springer, Berlin, 1999.
- [5] F. H. Lopes da Silva, W. Blanes, S. N. Kalitzin, J. Parra, P. Suffczynski, and D. N. Velis. Epilepsies as dynamical diseases of brain systems: basic models of the transition between normal and epileptic activity. *Epilepsia*, 44(Suppl. 12):72–83, 2003.
- [6] J. R. Brasic. Hallucinations. *Percep. Motor Skills*, 86:851–877, 1998.
- [7] S. H. Isaacson, J. Carr, and A. J. Rowan. Ciprofloxacin-induced complex partial status epilepticus manifesting as an acute confusional state. *Neurol.*, 43:1619
- [8] G. B. Ermentrout and J. D. Cowan. A mathematical theory of visual hallucination patterns. *Biol. Cybern.*, 34:137
- [9] V. K. Jirsa and H. Haken. Field theory of electromagnetic brain activity. *Physical Review Letters*, 7(5):960–963, 1996.
- [10] C. Uhl, editor. *Analysis of Neurophysiological Brain Functioning*. Springer-Verlag, Berlin, 1999.
- [11] A. Hutt and H. Riedel. Analysis and modeling of quasi-stationary multivariate time series and their application to middle latency auditory evoked potentials. *Physica D*, 177:203
- [12] H. Haken. *Principles of Brain Functioning*. Springer, Berlin, 1996.
- [13] W. J. Freeman. A model for mutual excitation in a neuron population in olfactory bulb. *IEEE Trans. Biomed. Engin.*, 21:350
- [14] J. C. Mosher, P. S. Lewis, and R. M. Leahy. Multiple dipole modeling and localization from spatio-temporal meg-data. *IEEE Trans. Biomed. Eng.*, 39(6):541
- [15] P. A. Robinson, P. N. Loxley, S. C. O’Connor, and C. J. Rennie. Modal analysis of corticothalamic dynamics, electroencephalographic spectra and evoked potentials. *Physical Review E*, 63:041909, 2001.
- [16] D. T. J. Liley, P. J. Cadusch, and M. P. Dafilis. A spatially continuous mean field theory of electrocortical activity. *Network: Comput. Neural Syst.*, 13:67–113, 2002.

- [17] W. Gerstner. Time structure of the activity in neural network models. *Phys. Rev. E*, 51(1):738–758, 1995.
- [18] P. C. Bressloff and S. Coombes. Physics of the extended neuron. *Int. J. Mod. Phys. B*, 11(20):2343–2392, 1997.
- [19] B. Ermentrout. Neural networks as spatio-temporal pattern-forming systems. *Reports on Progress in Physics*, 61:353–430, 1998.
- [20] W. M. Kistler, R. Seitz, and J. L. van Hemmen. Modeling collective excitations in cortical tissue. *Physica D*, 114:273–295, 1998.
- [21] R. Ben-Yishai, R. L. Bar-Or, and H. Sompolinsky. Theory of orientation tuning in visual cortex. *Proc. Natl. Acad. Sci.*, 92:3844
- [22] T. Wennekers. Dynamic approximation of spatio-temporal receptive fields in non-linear neural field models. *Neural Computation*, 14:1801–1825, 2002.
- [23] K. J. Friston. Transients, metastability and neuronal dynamics. *NeuroImage*, 5:164
- [24] J. Eggert and J. L. van Hemmen. Unifying framework for neuronal dynamics. *Phys. Rev. E*, 61(2):1855
- [25] S. Coombes and M. R. Owen. Evans functions for integral neural field equations with heaviside firing rate function. *SIAM J. Appl. Dyn. Syst.*, 3(4):574–600, 2005.
- [26] H. R. Wilson and J. D. Cowan. Excitatory and inhibitory interactions in localized populations of model neurons. *Biophys. J.*, 12:1–24, 1972.
- [27] P. L. Nunez. *Neocortical dynamics and human EEG rhythms*. Oxford University Press, New York - Oxford, 1995.
- [28] A. Hutt, M. Bestehorn, and T. Wennekers. Pattern formation in intracortical neuronal fields. *Network: Comput. Neural Syst.*, 14:351–368, 2003.
- [29] G. B. Ermentrout and J. Cowan. Large scale spatially organized activity in neural nets. *SIAM J. Applied Math.*, 38(1):1–21, 1980.
- [30] S. Amari. Dynamics of pattern formation in lateral-inhibition type neural fields. *Biol. Cybernetics*, 27:77–87, 1977.
- [31] K. Kishimoto and S. Amari. Existence and stability of local excitations in homogeneous neural fields. *J. Math. Biology*, 7:303–318, 1979.
- [32] R. Osan and G. B. Ermentrout. The evolution of synaptically generated waves in one- and two-dimensional domains. *Physica D*, 163:217–235, 2002.
- [33] F. M. Atay and A. Hutt. Stability and bifurcations in neural fields with finite propagation speed and general connectivity. *SIAM J. Appl. Math.*, 65(2):644–666, 2005.

- [34] S. M. Crook, G. B. Ermentrout, M. C. Vanier, and J. M. Bower. The role of axonal delays in the synchronization of networks of coupled cortical oscillators. *J. Comput. Neurosci.*, 4:161–172, 1997.
- [35] J. F. Vibert, F. Alvarez, and J. Pham. Effects of transmission delays and noise in recurrent excitatory neural networks. *Biosystems*, 48:255–262, 1998.
- [36] W. Gerstner. Population dynamics of spiking neurons: fast transients, asynchronous states, and locking. *Neural Computation*, 12:43–89, 2000.
- [37] W. J. Freeman. Characteristics of the synchronization of brain activity imposed by finite conduction velocities of axons. *Int. J. Bif. Chaos*, 10(10):2307–2322, 2000.
- [38] S. Coombes, G. J. Lord, and M. R. Owen. Waves and bumps in neuronal networks with axo-dendritic synaptic interactions. *Physica D*, 178:219–241, 2003.
- [39] A. Hutt. Effects of nonlocal feedback on traveling fronts in neural fields subject to transmission delay. *Phys. Rev. E*, 70:052902, 2004.
- [40] C. R. Laing, W. C. Troy, B. Gutkin, and G. B. Ermentrout. Multiple bumps in a neuronal model of working memory. *SIAM J. Appl. Math.*, 63(1):62–97, 2002.
- [41] C. R. Laing and W. C. Troy. PDE methods for nonlocal models. *SIAM J. Appl. Dyn. Syst.*, 2(3):487–516, 2003.
- [42] J. D. Cowan. Statistical mechanics of nervous nets. In E. Caianiello, editor, *Proceedings of 1967 NATO Conference on Neural Networks*, pages 181–188. Springer-Verlag, 1968.
- [43] H. R. Wilson and J. D. Cowan. A mathematical theory of the functional dynamics of cortical and thalamic nervous tissue. *Kybernetik*, 13:55–80, 1973.
- [44] V. K. Jirsa. Connectivity and dynamics of neural information processing. *Neuroinformatics*, 2(2):183–204, 2004. large review paper.
- [45] J. Cowan and G. Ermentrout. Some aspects of the ‘eigenbehavior’ of neural nets. In S. Levin, editor, *Studies in mathematical biology, part I: Cellular behavior and the development of pattern*, pages 67 Washington DC, 1978.
- [46] D. J. Amit. *Modeling brain function: The world of attractor neural networks*. Cambridge University Press, Cambridge, 1989.
- [47] J. C. Eccles, M. Ito, and J. Szentagothai. *The Cerebellum as a Neuronal Machine*. Springer-Verlag, New York, 1967.
- [48] W. J. Freeman. *Mass Action in the Nervous System*. Academic Press, New York, 1975.
- [49] P. Dayan and L. F. Abbott. *Theoretical Neuroscience : Computational and Mathematical Modeling of Neural Systems*. MIT Press, 2001.

- [50] J. Eggert and J. L. van Hemmen. Modeling neuronal assemblies: Theory and implementation. *Neural Comput.*, 13(9):1923
- [51] V. B. Mountcastle. Modality and topographic properties of single neurons of cat's somatic sensory cortex. *Neurophysiol.*, 20:408
- [52] D. H. Hubel and T. N. Wiesel. Receptive fields of cells in striate cortex of very young, visually unexperienced kittens. *J. Physiol.*, 26:994
- [53] K. J. Sanderson. The projection of the visual field to the lateral geniculate and medial interlaminar nuclei in the cat. *J. Comp. Neurol.*, 143:101
- [54] J. J. Wright and D. T. J. Liley. Dynamics of the brain at global and microscopic scales: Neural networks and the EEG. *Behavioral and Brain Sciences*, 19:285–320, 1996.
- [55] J. J. Wright. EEG simulation: variation of spectral envelope, pulse synchrony and approx. 40hz oscillations. *Biol. Cybern.*, 76:181–194, 1997.
- [56] B. Ermentrout. Reduction of conductance based models with slow synapses to neural nets. *Neural Computation*, 6:679–695, 1994.
- [57] W. J. Freeman. Tutorial on neurobiology: From single neurons to brain chaos. *International Journal of Bifurcation and Chaos*, 2(3):451–482, 1992.
- [58] W. Singer. Neural synchrony: A versatile code for the definition of relations? *Neuron*, 24:49–65, 1999.
- [59] B. Knight. Dynamics of encoding in a population of neurons. *J. Gen. Physiology*, 59:734–766, 1972.
- [60] C. van Vreeswijk and H. Sompolinsky. Chaos in neuronal networks with balanced excitatory and inhibitory activity. *Science*, 274:1724–1726, 1996.
- [61] B. S. Gutkin, G. B. Ermentrout, and J. O'Sullivan. Layer 3 patchy recurrent excitatory connections may determine the spatial organization of sustained activity in the primate prefrontal cortex. *Neurocomputing*, 32-33:391–400, 2000.
- [62] P. C. Bressloff, J. D. Cowan, M. Golubitsky, P. J. Thomas, and M. C. Wiener. What geometric visual hallucinations tell us about the visual cortex. *Neural Computation*, 14:473–491, 2002.
- [63] J. J. Wright. Simulation of EEG: dynamic changes in synaptic efficacy: cerebral rhythms, and dissipative and generative activity in cortex. *Biol. Cybern.*, 81:131–147, 1999.
- [64] C. J. Rennie, P. A. Robinson, and J. J. Wright. Unified neurophysical model of EEG spectra and evoked potentials. *Biological Cybernetics*, 86:457–471, 2002.
- [65] P. C. Bressloff. Bloch waves, periodic feature maps and cortical pattern formation. *Phys. Rev. Lett.*, 89:088101, 2002.

- [66] B. Katz, editor. *Nerve, Muscle and Synapse*. McGraw-Hill, New York, 1966.
- [67] A. M. Turing. The chemical basis of morphogenesis. *Philos. Trans. R. Soc. London*, 327B:37–72, 1952.
- [68] V. Castets, E. Dulos, J. Boissonade, and P. D. Kepper. Experimental-evidence of a sustained standing turing-type non-equilibrium chemical-pattern. *Phys. Rev. Lett.*, 64:2953–2956, 1990.
- [69] L. Perko. *Differential Equations and Dynamical Systems*. Springer, Berlin, 1998.
- [70] H. Haken. *Advanced Synergetics*. Springer, Berlin, 1983.
- [71] J. B. Swift and P. C. Hohenberg. Hydrodynamic fluctuations at the convective instability. *Phys. Rev. A*, 15:319, 1977.
- [72] M. C. Cross and P. C. Hohenberg. Pattern formation outside of equilibrium. *Reviews of Modern Physics*, 65(3):851–1114, 1993.
- [73] P. C. Matthews. Hexagonal patterns in finite domains. *Physica D*, 116:81–94, 1998.
- [74] T. Wennekers. Orientation tuning properties of simple cells in area v1 derived from an approximate analysis of nonlinear neural field models. *Neural Computation*, 13:1721–1747, 2001.
- [75] D. C. Somers, S. B. Nelson, and M. Sur. An emergent model of orientation selectivity in cat visual cortical simple cells. *J. Neurosci.*, 15(8):5448–5465, 1995.
- [76] J. Rinzel, D. Terman, X. J. Wang, and B. Ermentrout. Propagating activity patterns in large-scale inhibitory neuronal networks. *Science*, 279:1351
- [77] G. Tamas, E. H. Buhl, and P. Somogyi. Massive autaptic self-innervation of gabaergic neurons in cat visual cortex. *J. Neurosci.*, 17(16):6352
- [78] P. Levy. Sur certains processus stochastique homogènes. *Comp. Math.*, 7:283
- [79] W. Feller. *An introduction to probability theory and its applications*. Wiley, New York, 1966.
- [80] V. Bringuier, F. Chavane, L. Glaeser, and Y. Fregnac. Horizontal propagation of visual activity in the synaptic integration field of area 17 neurons. *Science*, 283:695–699, 1999.
- [81] J. J. Wright and D. T. J. Liley. A millimetric-scale simulation of electrocortical wave dynamics based on anatomical estimates of cortical synaptic density. *Biosystems*, 63:15–20, 2001.
- [82] B. Gough. *GNU Scientific Library Reference Manual*. Network Theory Ltd, 2 edition, 2003.
- [83] O. François, C. Larota, J. Horikawa, and T. Hervé. Diffusion and innovation rates for multidimensional neuronal data with large spatial covariances. *Network: Comput. Neural Syst.*, 11:211–220, 2000.

- [84] D. J. Pinto and G. B. Ermentrout. Spatially structured activity in synaptically coupled neuronal networks: I. travelling fronts and pulses. *SIAM J. Applied Math.*, 62(1):206–225, 2001.
- [85] A. K. Engel, O. Koenig, A. K. Kreiter, and W. Singer. Interhemispheric synchronization of oscillatory neuronal response in cat visual cortex. *Science*, 252:1177–1179, 1991.
- [86] M. Steriade, D. A. McCormick, and T. J. Sejnowski. Thalamocortical oscillations in the sleeping and aroused brain. *Science*, 262:679–685, 1993.
- [87] A. Knoblauch and F. T. Sommer. Synaptic plasticity, conduction delays, and interareal phase relations of spike activity in a model of reciprocally connected areas. *Neurocomputing*, 52-54:301–306, 2003.
- [88] P. A. Robinson, C. J. Rennie, and J. J. Wright. Propagation and stability of waves of electrical activity in the cerebral cortex. *Physical Review E*, 56(1):826–840, 1997.

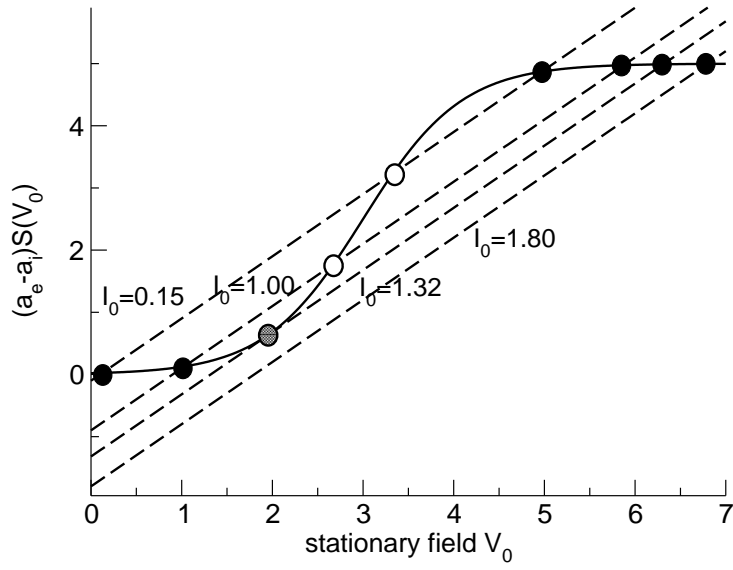


Figure 1: Illustration for the detection of constant stationary solutions of Eq. (11). For  $I_0 < 1.32$ , there are three solutions, while for  $I_0 > 1.32$  there is only a single one at large values of  $V_0$ . Filled circles represent stable fixed points, while empty circles illustrate unstable fixed points. At the critical value  $I = 1.32$ , there is a saddle node solution (hatched circle) synchronous to a stable fixed point at large values of  $V_0$ , cf. Fig. 2. Here, we applied the sigmoid function  $S = 1/(1 + \exp(-c(V - V_r)))$  [48, 88],  $a_e = 10$ ,  $a_i = 5$  and  $c = 1.8$ ,  $V_r = 3.0$  [81].

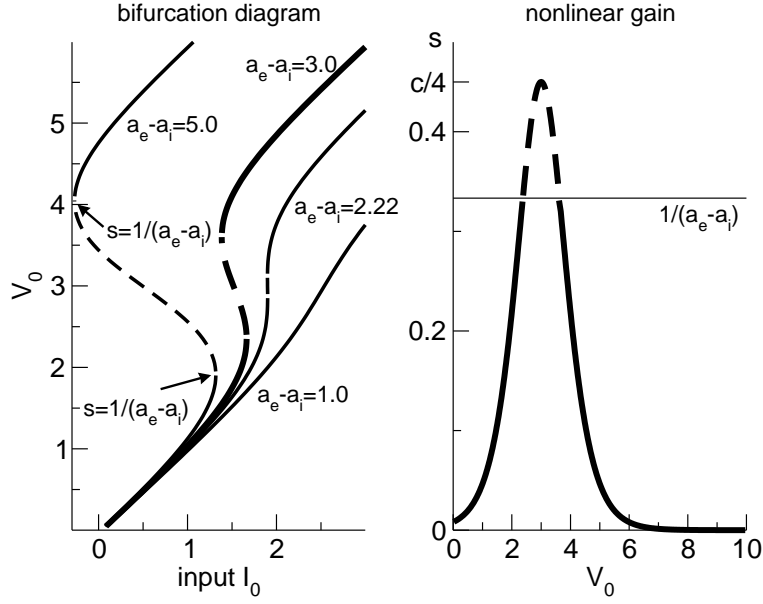


Figure 2: Bifurcation diagram and nonlinear gain for constant bifurcations for  $a_e > a_i$ . Left panel: Stability of the stationary state  $V_0$  with respect to external input  $I_0$ . For  $a_e - a_i > 4/c = 2.22$ , both stable (solid line) and unstable branches (dashed line) exist, while for  $a_e - a_i \leq 2.22$  there is only a single stable solution. Right panel: The nonlinear gain  $s$  with respect to the constant state  $V_0$ . The horizontal line  $s = 1/(a_e - a_i)$  separates stable from unstable states and determines the critical values of  $V_0$ . In both panels, we applied the sigmoid function introduced in Fig. 1.

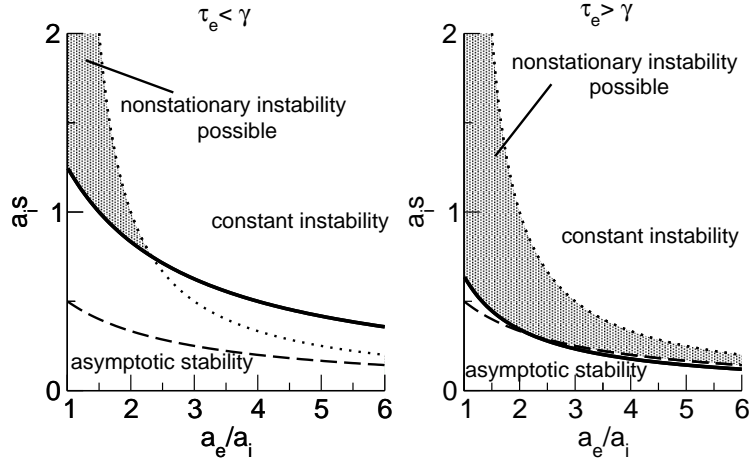


Figure 3: Necessary parameter regime for nonstationary instabilities for diverse mean excitatory interaction time  $\tau_e$  and synaptic delay constant  $\gamma$ . Valid parameters (hatched area) are constrained by the threshold of Eq. (21) plotted as solid line, the threshold of constant bifurcation (dotted line) and the threshold of asymptotic stability (dashed line).

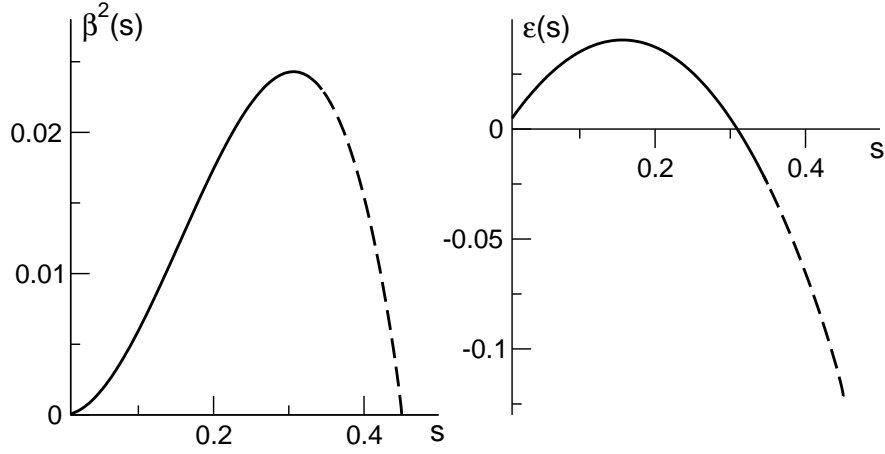


Figure 4: Expansion factors  $\beta^2$  and  $\epsilon$  plotted with respect to the control parameter  $s$ . The solid line part gives the parameter range of stable solutions  $V_0$ , for which Turing instabilities might occur. The dashed line part denotes the parameter domain of unstable stationary solutions  $V_0$ , cf. Fig. 2. In both panels  $a_e = 8$ ,  $a_i = 5.0$ , and we applied the sigmoid function introduced in Fig. 1.

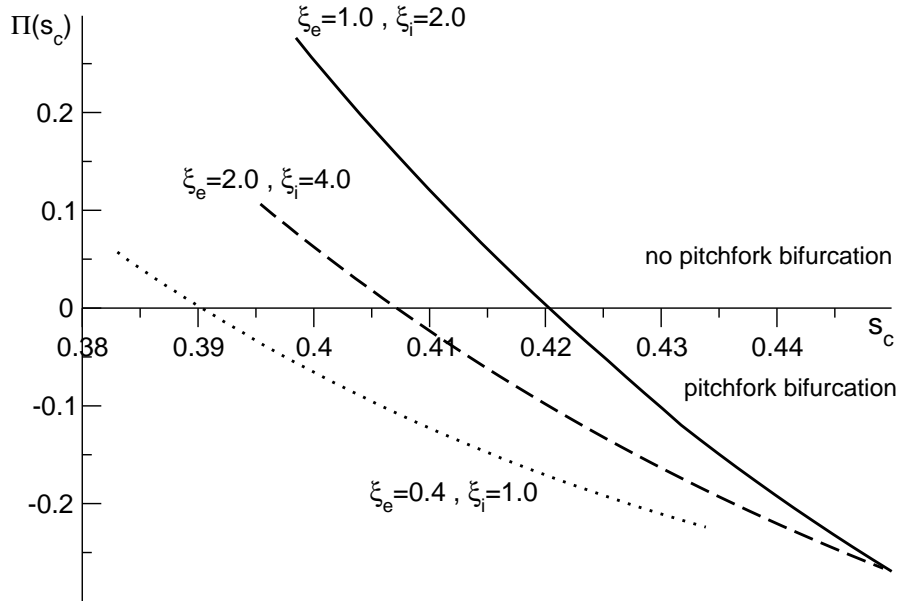


Figure 5: The factor  $\Pi$  of the cubic term in Eq. (36) plotted with respect to the bifurcation threshold  $s_c$  from Eq. (18) for various  $\xi_e, \xi_i$ . Each suitable parameter set  $a_e, a_i, \xi_e, \xi_i$  maps to a maximum of  $\hat{K}(k)$  and thus a single value  $s_c$ . Thus the plots have been computed by decreasing  $a_e$  leading to increasing  $s_c$ , while  $0 < a_e - a_i < 4/c$ . The range of  $a_e$  depends on  $\xi_e, \xi_i$ . The parameters have been chosen as  $a_i = 5.0$ ,  $\gamma = 2.1$  and the sigmoid function is as in Fig. 1.

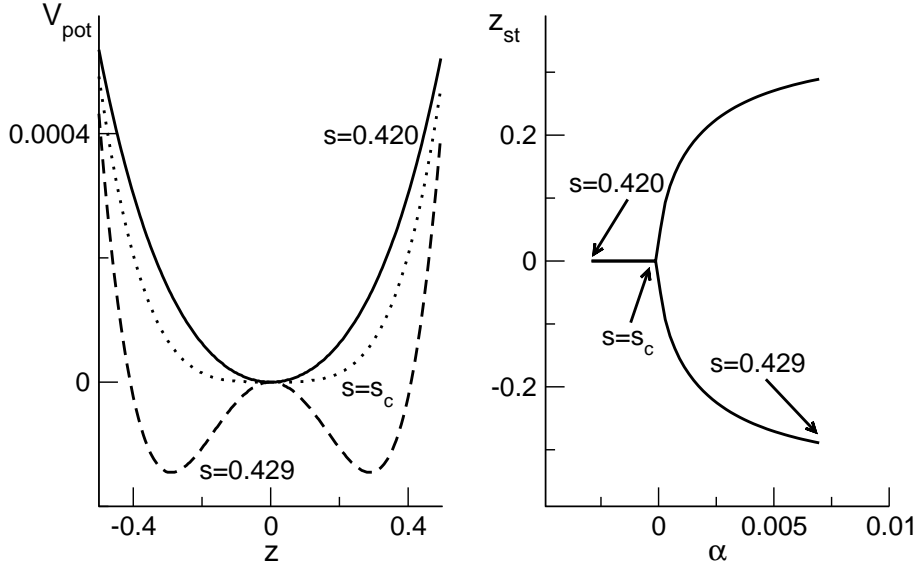


Figure 6: Potential  $V_{pot}$  and bifurcation diagram of the order parameter equation (36). It has been found that  $k_c = 0.6$ ,  $s_c = 0.423$  and  $V_0 = 2.723$  at  $s_c$  with parameters  $a_e = 6.0$ ,  $a_i = 5.0$ ,  $\xi_e = 1.0$ ,  $\xi_i = 2.0$ ,  $\gamma = 2.1$  and the sigmoid function from Fig. 1.

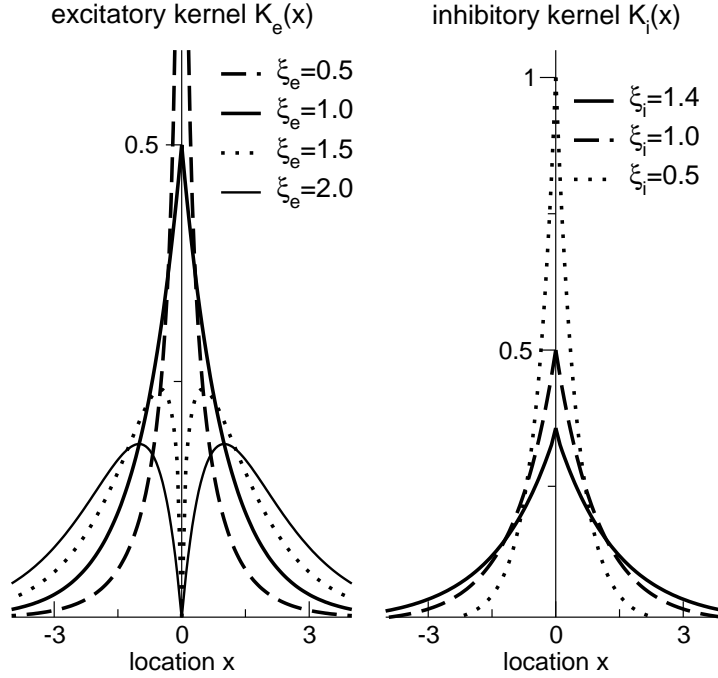


Figure 7: Excitatory and inhibitory kernels for various parameters. All kernels are finite except for  $K_e(x)$  for  $p = 0.5$ . In the case of  $\xi_e > 1$ , the excitatory kernel  $K_e(x)$  exhibits a maximum at  $x = \xi_e - 1$ . We point out that  $\xi_e < 1$  yields divergent excitatory self-connectivity, while the excitatory self-connectivity vanishes for  $\xi_i > 1$ .

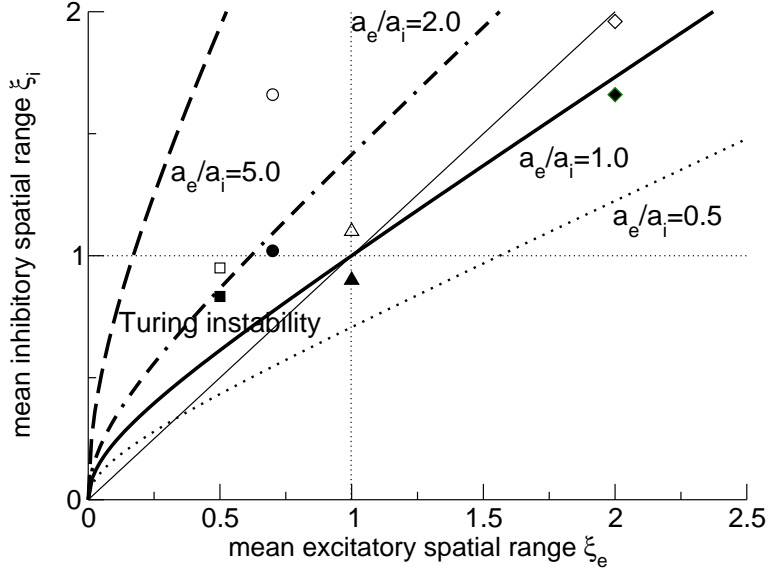


Figure 8: Sufficient parameter regimes of Turing patterns with respect to spatial interaction ranges  $\xi_i$ ,  $\xi_e$  and various values of  $a_e/a_i$ . The thin solid line denotes  $\xi_i = \xi_e$ , while filled and empty squares, triangles and diamonds mark different cases discussed in Figs. 9 and 10.

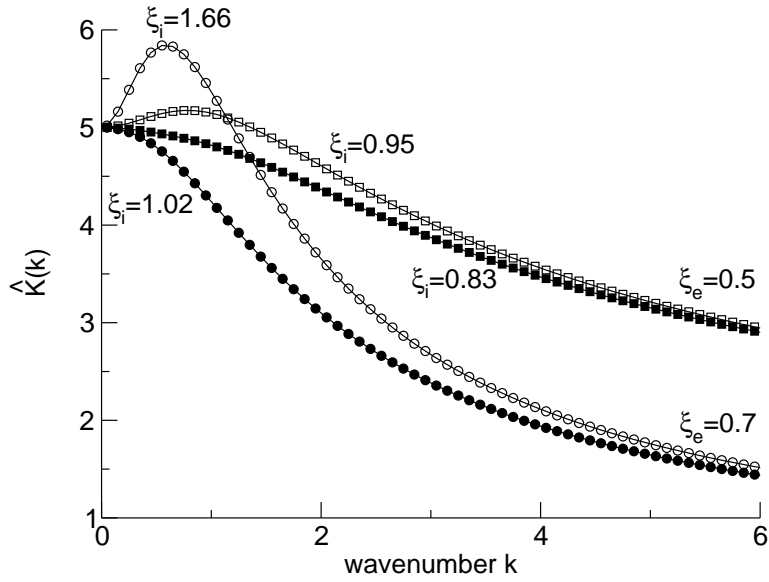


Figure 9: Function  $\hat{K}(k)$  for  $\xi_e < \xi_i$ . Parameter values are chosen according to Fig. 8. Both values of  $\xi_e$  allow a local maximum of  $\hat{K}(k)$  for  $k > 0$  and thus facilitate Turing patterns. Here,  $a_e = 10$  and  $a_i = 5$ .

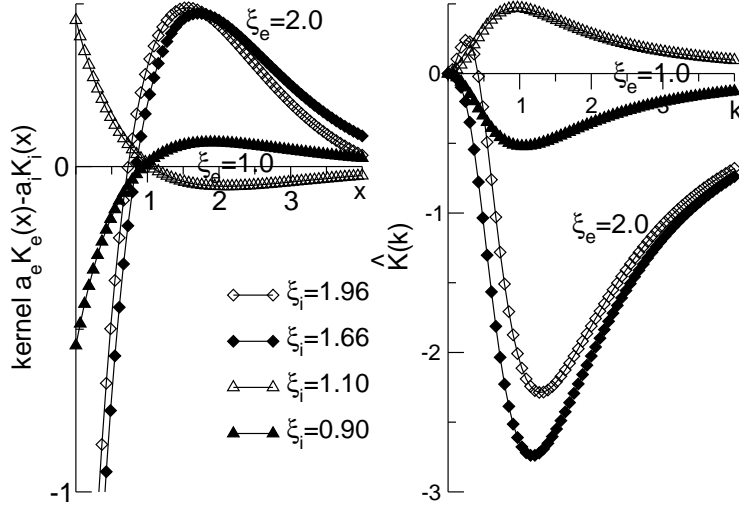


Figure 10: The kernel function  $a_e K_e(x) - a_i K_i(x)$  and the function  $\hat{K}(k)$  for  $\xi_e \geq \xi_i$ . Parameter values are chosen according to Fig. 8. In the case of  $\xi_e = 1.0$ , local excitation-lateral inhibition ( $\xi_i = 1.10$ ) yields a local maximum of  $\hat{K}$ , i.e. Turing patterns, while local inhibition-lateral excitation ( $\xi_i = 0.90$ ) prohibits Turing patterns. In contrast,  $\xi_e = 2.0$  exhibits local inhibition-lateral excitation for both values of  $\xi_i$ , while  $\hat{K}$  shows a local maximum for  $\xi_i = 1.96$ . Here,  $a_e = 5, a_i = 5$ .

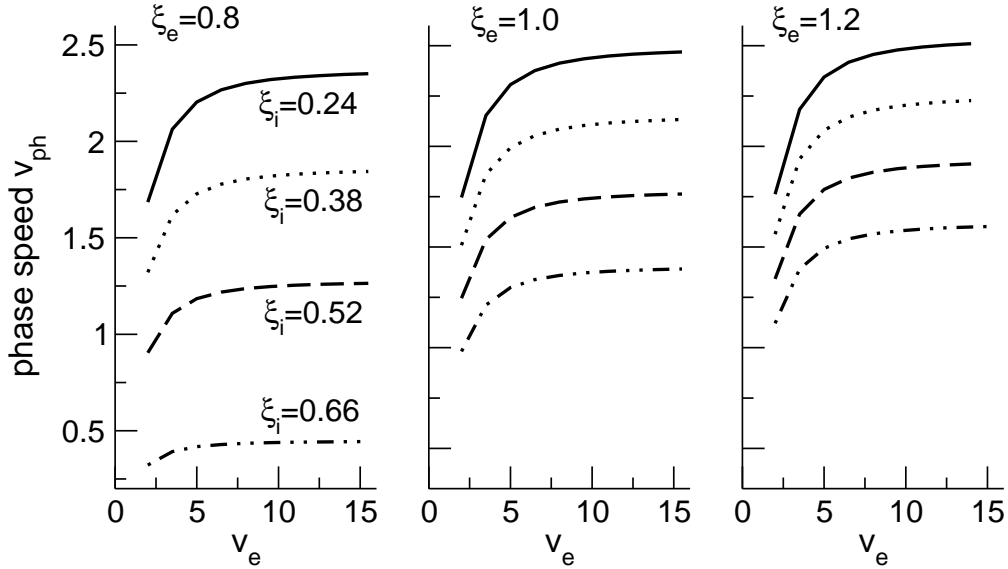


Figure 11: Plots of the traveling wave speed  $v_{ph}$  with respect to the transmission speed  $v_e$  for various parameters  $\xi_e, \xi_i$ . For  $\xi_e < 1$ , the field reveals traveling waves for local excitation and lateral inhibition, which strongly contrasts to previous findings. The plots show an increase of  $v_{ph}$  by decreasing the inhibitory range  $\xi_i$  and increasing the excitatory range  $\xi_e$ . The applied parameters are  $a_e = 60, a_i = 55, v_i = 100$  and  $\gamma = 2.1$ .

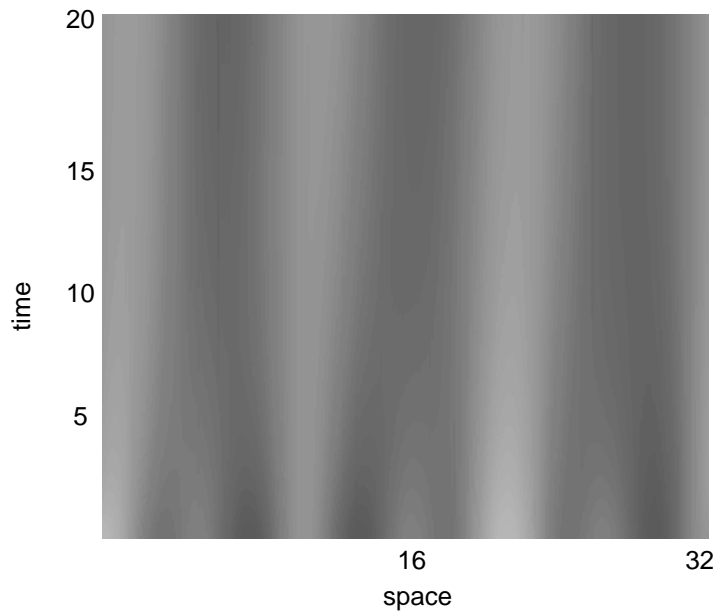


Figure 12: Space-time plot revealing the Turing instability for local excitation-lateral inhibition interaction. Parameters are set to  $\xi_e = 1.0$ ,  $\xi_i = 2.0$ ,  $a_e = 6.0$ ,  $a_i = 5.0$ ,  $v_e = 10.0$  with external stimulus  $I_0 = 2.36$  yielding  $V_0 = 2.75$  and  $s_c = 0.428, k_c = 0.589$ . The temporal evolution is calculated with time increment  $dt = 0.01$  while the space is discretized with  $dx = 0.08$ ,  $N = 400$ . The greyscale encodes the deviation from the stationary state. The resulting pattern wavenumber agrees well with  $k_c$ .

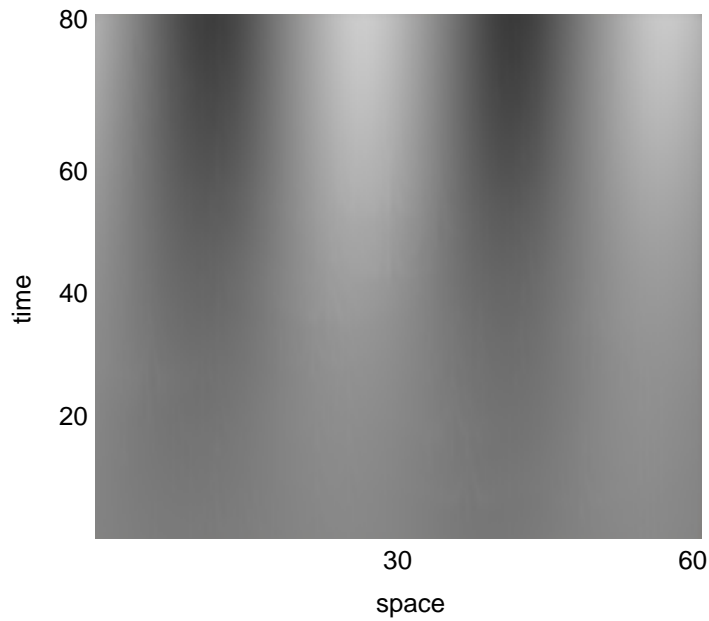


Figure 13: Space-time plot revealing the Turing instability for local inhibition-lateral excitation interaction. Parameters are set to  $\xi_e = 2.0$ ,  $\xi_i = 1.92$ ,  $a_e = 131.0$ ,  $a_i = 130.0$ ,  $v_e = 10.0$  with external stimulus  $I_0 = 2.2$  yielding  $V_0 = 2.48$  and  $s_c = 0.365$ ,  $k_c = 0.24$ . The temporal evolution is calculated with the time increment  $dt = 0.01$  while the space is discretized with  $dx = 0.15$ ,  $N = 400$ . The greyscale encodes the deviation from the stationary state. The resulting pattern wavenumber agrees well with  $k_c$ .